Plasma Detachment in Divertor Tokamaks

A.W. Leonard[1]

[1]*General Atomics, San Diego, CA, USA*

Leonard@fusion.gat.com

Abstract

Observations of divertor plasma detachment in tokamaks are reviewed. Plasma detachment is characterized in terms of transport and dissipation of power, momentum and particle flux along the open field lines from the midplane to the divertor. Asymmetries in detachment onset and other characteristics between the inboard and outboard divertor plasmas is found to be primarily driven by plasma $\vec{E}\times\vec{B}$ drifts. The effect of divertor plate geometry and magnetic configuration on divertor detachment is summarized. Control of divertor detachment has progressed with a development of a number of diagnostics to characterize the detached state in real-time. Finally the compatibility of detached divertor operation with high performance core plasmas is examined.

I. Introduction

Investigation of highly dissipative boundary plasmas in divertor tokamaks began in earnest in the 1990's when the first designs for ITER called for 80% -90% of the exhaust power to be dissipated before intercepting the divertor target [1]. With future Demo designs at even higher power densities much greater reductions of target heat and particle flux will be needed to not exceed material limitations [2,3]. Initial experiments to reduce divertor heat flux, carried out in JET[4], ASDEX-Upgrade[5-7], DIII-D[8-11], JT-60U[12] and C-Mod[13-15] obtained success with significantly increased divertor radiation through additional gas fueling to raise density and lower divertor plasma temperature. These divertor plasmas were labeled as "detached" as the primary plasma boundary interaction moved upstream off the divertor target surface[16].

Plasma detachment can be more quantitatively defined as a significant loss term in the continuity equation for energy, momentum and particle flux parallel to the magnetic field lines from the midplane Scrape-Off-Layer (SOL) to the divertor target. While dissipation of energy is the primary goal for detached divertors, the dissipation of pressure upstream of the target is also important in order to reduce the ion flux and associated ionization energy of recombination within the material surface [17,18]. Finally plasma recombination within the divertor plasma may also aid in reducing target particle and associated energy fluxes.

The role of energy and momentum losses on detached divertor plasma conditions can be expressed in terms of the modified Two-Point Model (2PM) [19].

$$T_t = \frac{q_{\parallel}^2}{n_{sep}^2}\left(\frac{2\kappa_e}{7q_{\parallel}L_{\parallel}}\right)^{4/7}\frac{2m_i}{\gamma^2 e^2}\frac{\left(1-f_{pow}\right)^2}{(1-f_{mom})^2(1-f_{conv})^{4/7}} \quad (1)$$

$$n_t = \frac{n_{sep}^3}{q_{\parallel}^2}\left(\frac{7q_{\parallel}L_{\parallel}}{2\kappa_e}\right)^{6/7}\frac{\gamma^2 e^3}{4m_i}\frac{(1-f_{mom})^3(1-f_{conv})^{6/7}}{\left(1-f_{pow}\right)^2} \quad (2)$$

$$\Gamma_t = \frac{n_{sep}^2}{q_{\parallel}}\left(\frac{7q_{\parallel}L_{\parallel}}{2\kappa_e}\right)^{4/7}\frac{\gamma e^2}{2m_i}\frac{(1-f_{mom})^2(1-f_{conv})^{4/7}}{\left(1-f_{pow}\right)} \quad (3)$$

where T_t, n_t, and Γ_t are the divertor target electron temperature, electron density and ion flux respectively, $q_{//}$ and n_{sep} are the upstream parallel electron heat flux and separatrix electron density, $L_{//}$ is the parallel connection length from midplane to target, γ is the sheath transmission coefficient, κ_e is the parallel electron heat conductivity constant and m_i is the ion mass. For the loss terms f_{pow} represents the fraction of parallel heat flux dissipated in the SOL from the midplane to the divertor target while f_{mom} represents similar dissipation of total plasma pressure and f_{conv} is the fraction of heat flux carried by parallel convection.

These expressions relate the divertor target conditions to the upstream values of parallel heat flux and plasma density, and describe how energy and momentum (pressure) losses affect the upstream/downstream relationship. Not only does the radiated power fraction reduce the target heat flux but also the target electron temperature. However a loss of plasma pressure, f_{mom}, or to some extent parallel convection, is required to reduce the target ion flux that would otherwise contribute to target heat flux through its ionization potential. While the 2PM provides a useful guideline for understanding how energy and momentum dissipation affect the divertor target conditions, it is not predictive of those losses. Predictive capability for detached divertor conditions requires 2D models that capture the appropriate dissipative and transport processes in an accurate geometric framework. The progress in development of such models is presented in the companion paper by Canik and Groth [20].

This review will summarize experimental observations of divertor detachment in tokamaks. The results are organized first with respect to observations of energy dissipation in Section II, momentum dissipation in Section III, and evidence of particle flux dissipation due to plasma recombination in Section IV. The resulting parallel transport in detached divertor plasmas is presented in Section V. Factors affecting characteristics of divertor detachment are also summarized with the effect of plasma drifts on divertor asymmetry in Section VI. Detachment interaction with ELM transients is discussed in Section VII. The role of divertor geometry on detachment is summarized in Section VIII. The stability and control of divertor detachment is discussed in Section IX. Finally the compatibility of divertor detachment with high core plasma confinement and overall performance is summarized in Section X. Further aspects of divertor detachment are summarized in a series of companion papers. Detachment in advanced divertor configurations is more thoroughly summarized in a review by Souhkanovskii [21] as is the topic of detachment with 3D fields by Ahn [22]. A theoretical consideration of plasma detachment can be found in the companion paper by Stangeby. [23] The progress of describing and predicting detachment with realistic models is summarized by Canik and Groth [20]. As briefly summarized in Section XI, the goal of this review is to provide a database of experimental observations of divertor detachment in order to guide and test the development of theory and models for predicting divertor detachment in future tokamaks.

II. Energy detachment

The study of detached divertors began in the mid 1990's in a number of tokamaks [16] including DIII-D [9,24-26], ASDEX-Upgrade [5,6], Alcator C-Mod [13,15,27], JET [4,28] and JT-60U [12,29]. A number of similarities with detached divertor plasmas have been observed across devices, as illustrated in the example from DIII-D in Fig. 1[9]. After H-mode is established with auxiliary heating, additional deuterium gas puffing raises the density resulting in a sharp increase in divertor radiation and drop in peak divertor heat flux. Peak heat flux reductions of a factor of 3 or more are typical with detachment onset. Fig. 2[9] shows the outer divertor target heat flux profile before gas injection with the solid line and after divertor detachment onset with the dashed line. While the heat flux at the strike-point is greatly reduced a few cm outside the strike-point the heat flux remains at the pre-gas injection level. This condition has been labeled "Partially Detached Divertor" due the detachment at the target plate extending only partially into the SOL.

A large increase in divertor radiation is also typically observed with divertor detachment as shown with examples from C-Mod [27] and DIII-D [30] shown in Figs. 3a and 3b respectively. Typically at detachment onset, outboard divertor radiation increases strongly within the entire divertor region as shown in these figures. With additional gas injection the high radiation region moves up off the target plate and coalesces around the X-point as shown in Fig. 3c from ASDEX-Upgrade [31]. Under these conditions the radiative losses now inside the separatrix often lead to degradation of the pedestal pressure in H-mode and lower overall confinement [24,31]. Whether this degradation is tolerable in future DEMO scenarios is still under investigation as will be discussed in Section X.

Intrinsic impurities typically make a significant contribution to radiative losses in in tokamaks with low-Z Plasma Facing Components (PFCs). These contributions were first quantified in JT-60U through VUV (Vacuum Ultra-Violet) spectroscopic analysis [32,33]. In neutral beam heated discharges both deuterium and intrinsic carbon impurity from the graphite walls contributed significantly to the total radiation as shown in Fig. 4. For deuterium the radiative losses were from ground state transitions of DI with some additional power loss due to charge-exchange with neutral deuterium. For the carbon impurity the radiative loss was primarily from the Li-like CIV charge state with some contributions from CIII. The total radiative losses through these channels were consistent with bolometric measurements of total radiated power. A similar conclusion was made for the ASDEX-Upgrade carbon LYRA divertor [34-36] where carbon was also determined to be the dominant radiator at ~60% of the total. The ASDEX-Upgrade analysis also found the total radiation from carbon is increased by roughly a factor of two above that expected from coronal equilibrium due to carbon impurity transport effects[35].

Analysis of UV spectroscopy in DIII-D confirmed the important contributions of carbon radiation, but also provided the spatial distribution of the radiating species [30,37]. By sweeping a detached divertor plasma through the field of view of a VUV spectrometer, carbon radiation, primarily CIV, was found to be dominant near the X-point to half-way down the divertor leg towards the target. Line-ratio analysis implied CIV radiation was dominant in the region of T_e ~9-11 eV, and CIII in the region of Te ~6-8 eV. Near the strike-point deuterium radiation became dominant in the region of $T_e \leq 5$ eV. Tangential images of CIII and Dα confirmed the spatial distribution of the carbon and deuterium radiation and divertor Thomson scattering measurements [38] confirmed the T_e in the region of peak emissivity respectively for each species.

As described above low Z impurity radiation is an important part of power dissipation in detached divertor operation. In tokamaks with low-Z PFCs, typically carbon, the impurity influx is primarily due to physical sputtering during low density attached divertor operation. For high density detached operation where T_e drops below the physical sputtering threshold, impurity influx becomes dominated by chemical sputtering in regions where the ion flux remains high. [35,39,40]. A review of chemical sputtering of carbon in tokamaks with graphite PFCs can be found in Roth [41]. Carbon erosion yields for chemical sputtering are also measured and modeled to decrease sharply for ion energies below 10 eV and at the higher flux densities of detached plasmas, $\Gamma \geq 10^{22} m^{-3}$. While this might suggest that carbon impurity density should decrease in detached plasmas with dense divertor conditions and $T_{e,div} \leq 5$ eV, typically intrinsic impurity density does not change significantly at detachment onset. Additionally, observations that the divertor is a region of net carbon deposition in DIII-D detached plasmas [42] suggests that impurity sources from the main chamber and divertor entrances play an increased role for detached divertor conditions.

For tokamaks with high Z PFCs, such as C-Mod [27], ASDEX-Upgrade after the PFC changeover to tungsten [31] and the JET ITER-Like-Wall (ILW) [43,44], injection of low Z impurities, typically nitrogen or neon, is used to produce sufficient radiation to achieve divertor detachment. While the physical processes of divertor detachment are measured to remain similar, between carbon and nitrogen for example, the dynamics and control of detachment can be quite different between tokmaks with intrinsic impurities from low-Z PFCs and those with high-Z PFCs requiring impurity injection. A few of these aspects are described in Section VIII on detachment control and stability.

III. Momentum detachment

Detached plasmas also typically exhibit a reduction in ion flux to the divertor target. This reduction is not only important for reducing erosion of the target, but also for surface heat flux due to atomic and molecular recombination of the ionization potential. Fig. 5 shows the divertor ion flux as a function of line-averaged density in a JET L-mode discharge measured by Langmuir probes [4]. While H-mode is considered more relevant due to its higher SOL and divertor power density, L-mode was chosen for this analysis due to its quiescence from lack of transient ELMs and the capability to carry out significant density scans in a single discharge. Similar reductions in ion flux have been observed in most tokamaks in ohmic, L-mode and H-mode discharges between ELMs.

The reduction of ion flux with divertor detachment was originally quantified as Degree of Detachment (DOD) with the JET data in Ref [4]. As shown in Eq. 3 from the Two Point model, the target ion flux is expected to scale with the square of the upstream density, $\Gamma_i \propto n_{sep}^2$. The DOD is then defined as $DOD \equiv \frac{C_0 n_{sep}^2}{\Gamma_i} = \frac{C_1 \bar{n}_e^2}{\Gamma_i}$ where $\bar{n}_e$ is the line-averaged electron density, the constant C_1 is determined by the target ion flux for low density attached divertor conditions and the line-averaged density is assumed to be a fixed factor times the separatrix density. An illustration of the ion flux falling below the $\bar{n}_e^2$ 2PM scaling with increasing density is shown in Fig. 5. Also note that once Γ_i falls below this scaling Γ_i drops in absolute value for only a small increase in density. Therefore, the onset of divertor detachment in tokamaks has often been quoted as the point where divertor ion flux rolls over and begins to decrease, and thereby alleviating the need to evaluate DOD with a separate density scan to determine the constant C_1.

From Eq. 3, an ion flux reduction below that expected from the 2PM, DOD > 1, implies a loss of plasma pressure, or momentum from the midplane to the divertor target. And in confirmation the original JET data exhibits a clear correlation between a high DOD and parallel electron pressure loss as measured by midplane and divertor target Langmuir probes [4]. Electron pressure loss along magnetic field lines from the midplane to the target has been investigated in a number of tokamaks as a fundamental aspect of divertor detachment. A clear demonstration of pressure loss with detached plasmas is shown in Fig. 6 from an ohmic discharge in Alcator C-Mod [45,46]. At low density in the sheath limited regime electron pressure is balanced across the SOL between midplane and divertor target Langmuir probes. Here the divertor electron pressure is normalized by a factor of 2 to account for the dynamic pressure of sonic flow into the sheath at the target. At higher density, in a high recycling regime T_e at the target, $T_{e,div}$, is reduced to ≤10 eV, yet the electron pressure remains balanced. Finally, when $T_{e,div}$ drops below 5 eV the divertor electron pressure drops a factor of 10 or more below that of the midplane. This drop occurs in the near SOL with pressure balance still maintained in the far SOL. Similar profiles of divertor electron pressure loss have been reported from JT-60U [47,48], DIII-D [49,50] and ASDEX Upgrade [51].

Electron pressure loss was examined in more detail as a function of $T_{e,div}$ in C-Mod [46] as shown in Fig. 7. At approximately $T_{e,div}$= 5 eV the divertor electron pressure begins to drop below that of the midplane. At $T_{e,div}$= 2 eV the divertor pressure is only 10% that of the midplane. Finally at $T_{e,div}$= 1 eV the divertor electron pressure has dropped to 1% that of the midplane. For this data scan the pressure drop was a the same function of $T_{e,div}$ at all radial locations. In an analysis of ASDEX-Upgrade data similar large electron pressure loss was measured in H-mode discharges along field lines close to the separatrix and low values of $T_{e,div}$, ≤ 2 eV [51]. However in contrast to the C-Mod data, with increasing distance from the separatrix momentum dissipation becomes increasingly less effective for the same value of $T_{e,div}$, with the 10 mm field line requiring $T_{e,div} \leq 3$ eV to obtain a 50% pressure loss. The correlation and parameterization of pressure dissipation with $T_{e,div}$ is examined in more detail in the companion paper by Stangeby [23].

The characteristics of electron pressure in detached plasmas are consistent with momentum dissipation dominated by neutral-ion interactions, primarily charge exchange and elastic scattering [52]. A simple model of this process is described in Self and Ewald [53],

$$f_{mom}(T_t) = \left(\frac{\alpha}{\alpha+1}\right)^{(\alpha=1)/2} \qquad (4)$$

where $\alpha \equiv \langle\sigma v\rangle_i / (\langle\sigma v\rangle_i + \langle\sigma v\rangle_m)$ and $\langle\sigma v\rangle_i$ and $\langle\sigma v\rangle_m$ are respectively the rate coefficients for ionization and momentum removal via charge exchange. Fluid modeling [51,54]confirms that below 10 eV, where the ionization rate begins to drop significantly, plasma momentum can be effectively dissipated into the recycling neutrals. Radial diffusion plays a small role as the integral of the target profile of pressure and ion flux is greatly reduced, not just the peak values. Modeling has also suggested a strong correlation between the divertor target neutral density and low $T_{e,div}$ associated with significant pressure dissipation [44,55]. Experimental confirmation of target neutral density is more challenging as most neutral measurements are made with pressure gauges removed from direct interface with the divertor target plasma. These measurements though have been used to infer target neutral density through modeling as summarized in the companion paper by Canik and Groth [20]. However a few spectroscopic measurements of divertor neutral emission find general agreement with the neutral density required to dissipate plasma pressure to the extent observed [56].

One large uncertainty in the description of plasma pressure balance in detached plasmas is the role of the ions in total plasma pressure balance. Limited measurements of ion temperature, T_i, in the midplane SOL suggest that T_i can be a factor of ≥ 2-3 higher than T_e [57]. Indications of higher electron pressure in the divertor than the midplane for ASDEX-Upgrade [51] and DIII-D [50,58] suggest a higher T_i at the midplane becomes thermally equilibrated to T_e at the divertor target. A lack of divertor electron overpressure in the C-Mod data of Fig. 7 may be due to its higher density where midplane thermal equilibration, $T_i=T_e$, is more likely to hold. Ion pressure is further complicated by the neoclassical effects of large ion poloidal gyro-radius orbits [59], and the potential for a fast ion component due to auxiliary heating. Additional measurements and analysis will be required to quantify the role of ion energy and momentum transport in detached divertor conditions.

IV. Particle Detachment through Plasma recombination

An ultimate goal of detached divertor operation is to remove plasma interaction with the divertor target to the greatest extent possible. The original gas target divertor concept relied on plasma-neutral interactions to remove plasma energy, momentum and ion flux [17,18]. Plasma recombination was thought to be a difficult process to achieve for plasma dissipation due to the low temperature requirement, $T_e \leq 1$ eV, and the somewhat higher typical $T_{e,div}$ measurements from divertor Langmuir probes, $T_e \sim 5$ eV. However, visible spectroscopy of C-Mod dense divertor plasmas revealed strong Balmer series emission from upper states, n=5 to n=11, indicating a dominance of recombination over ionization [60]. In addition, analysis of the continuum radiation from bremsstrahlung and recombination revealed a low $T_{e,div}$ of 0.8-1.5 eV. In addition to three body recombination ($e + e + D^+ \Rightarrow D_0 + e$) radiative recombination ($e + D^+ \Rightarrow D_0 + h\nu$) was found to contribute an additional ~5% to the total recombination rate. The spectroscopic observation of plasma recombination was confirmed in a number of other tokamaks with detached divertor plasmas, including DIII-D [61], JT-60U [62,63], ASDEX-Upgrade [64,65], JET [66,67] and NSTX [68]. In DIII-D the low T_e values, $T_e \leq 1$ eV, in detached plasmas required for these processes were subsequently directly measured by Thomson scattering [38].

Further spectroscopic analysis has suggested that Molecular Activated Recombination (MAR) may also be playing an important role in the total rate of plasma recombination [63,69,70]. The MAR process ($D_2^+ + e \Rightarrow D_0 + D_0$) occurs when recycled deuterium molecules are ionized and then recombine. This process is expected to be dominant in a range of about 0.8 – 2.0 eV and could be a key factor in reducing $T_{e,div}$ to ≤ 1.0 eV where three body recombination can take over. Evidence for MAR was observed by measurements of Fulcher band molecular emission in JT-60U [63].

In Alcator C-Mod a radiative-collisional model was used to convert the magnitude of $D\gamma$ emission into a total ion recombination rate [70,71]. As shown in Fig. 8, recombination was able to account for up to 75% of the total divertor ion sink in L-mode detached divertor conditions, with the remainder, 25%, flowing to the target as ion flux. In C-Mod and ASDEX-Upgrade [65] VUV spectroscopy revealed that the high neutral density can be opaque to Lyman series emission from the recombining plasma and thereby significantly reduce the recombination rate. Such radiative trapping will be an important consideration for heat flux control in future higher power density tokamaks.

V. Transport in detached plasmas

The 2D measurements of divertor density and temperature with Thomson scattering in DIII-D have allowed the examination of important transport processes in detached plasmas. Fig. 9 from DIII-D shows the 2D profile of n_e and T_e in a detached H-mode divertor plasma [50]. These profiles from Thomson scattering were obtained by magnetically sweeping the divertor plasma across an 8-channel view of a vertical laser beam [38]. Profiles from divertor target Langmuir probes and Dα emission indicate the plasma conditions remained constant during the sweep. The Thomson scattering data exhibit a very low T_e, ≤ 1 eV, and high $n_e \geq 10^{20}$ m^{-3}, along the target. About 5-10 cm above the target the plasma transitions to a region with T_e in the 6-12 eV range, but with a significantly lower n_e, $\sim 5x10^{19}$ m^{-3}. The two regions correspond to high deuterium radiation and carbon radiation respectively, as described earlier in Sec II. The 2D divertor profiles, such as those in Fig. 9, have been examined in terms of parallel transport processes by collating data as functions of radial magnetic flux surface and parallel distance along the magnetic field line from the divertor target [72,73]. The parallel heat flux, $q_{||}$, is determined from the divertor target heat flux profile and integrating the 2D radiation profile in the SOL, measured by bolometry, from the target to the midplane. For lower density attached plasmas, $T_{e,div} \geq 10$ eV, the T_e profile from the target to the midplane is consistent with electron thermal conduction, $q_{\parallel,cond} = \kappa_0 T_e^{5/2} \frac{dT_e}{ds}$ as shown in Fig. 10a. However, due to the strongly nonlinear dependence on temperature the low T_e and its gradient in detached divertor plasmas can support only very low levels of parallel conduction, Fig. 10b. The power can, though, be carried by parallel convection, $q_{\parallel,conv} = nv_{\parallel}\left(\frac{5}{2}(T_i + T_e) + \frac{1}{2}m_i v_{\parallel}^2 + I_0\right)$, where $v_{\parallel}$is the parallel fluid velocity and I_0 is the atomic ionization and molecular dissociation potential, 13.6 eV + 2.2 eV for deuterium. In this analysis parallel plasma flow at near the sound speed for regions of $T_e \leq 10$ eV is consistent with the levels of observed parallel heat flux.

Confirmation of near sonic flow in detached divertor plasmas has been made in several tokamaks. In JT-60U [74], ASDEX-Upgrade [75] and DIII-D [76,77] insertable Mach probes in the outboard divertor have found parallel plasma flow approaching sonic speed as the density was raised to divertor detachment. Sonic parallel plasma flow in detached divertor plasmas were also observed with spectroscopy in DIII-D [78]. The Doppler shift of carbon impurities, primarily CII and CIII, generally indicate an increase in velocity towards the divertor target with the transition to detached conditions. The Doppler shift of Balmer emission from neutral deuterium atoms that have been thermalized with the back ground plasma also indicate deuteron ion velocities near sonic speed.

The observation of parallel convection carrying the parallel heat flux, rather than conduction, in detached divertor plasmas is significant in that it implies a much greater potential for dissipation of exhaust heat and particle flux. For conduction dominated parallel transport the parallel length, or volume, of plasma with $T_e \leq 10$ eV is very small due to the strongly nonlinear T_e dependence. This would imply a significant limitation on the volume of efficient radiating conditions and the total fraction of exhaust power that could be dissipated in a reactor scale tokamak [79,80]. Significant parallel convection greatly expands the volume of $T_e < 10$ eV, providing for much greater levels of low-Z radiation. Convection also expands the region where neutral charge-exchange, elastic ion collisions and plasma recombination can effectively dissipate plasma momentum and particle flux. The accuracy to which 2D models can describe this process of upstream ionization driving parallel flow, resulting in enhanced dissipation due to atomic processes and neutral interactions is described in the companion paper by Canik and Groth [20].

A simple model of parallel transport can be combined with the dissipation processes discussed in the previous sections to determine the requirements for detachment in terms of the divertor neutral pressure. Such a model can be motivated by the empirical observation from ASDEX-Upgrade shown in Fig. 11 [31]. In a series of scans of deuterium fueling and nitrogen seeding, divertor detachment with $T_{e,div} \leq 5$ eV was achieved when a detachment qualifier, q_{det}, fell below a value of 1, where q_{det} is given by

$$q_{det} = \frac{1.3\times P_{sep}}{R(p_0+18p_{0,N})} \qquad (5)$$

with P_{sep} the power across the separatrix in MW and p_0 and $p_{0,N}$ the divertor netural pressures of deuterium and nitrogen respectively. The total neutral pressure was measured by a pressure gauge in the divertor region with the nitrogen pressure inferred from the ratio of injection valve fluxes of deuterium and nitrogen. The factor of 18 for nitrogen pressure was motivated by the higher radiation efficiency compared to deuterium.

This empirical observation relating detachment to divertor neutral pressure is captured in a 1D model of parallel transport by electron conduction and ionization driven convection with atomic physics rates taken from the ADAS database for ionization, charge-exchange and radiation dissipation with estimates for non-coronal effects [81]. The resulting model predicts a detachment onset operating point given by

$$P_{sep}/R = \frac{p_0(1+f_z c_z)}{1.3}\left(\frac{\lambda_q}{0.005m}\right)\left(\frac{R}{1.65m}\right)^{r_z} \qquad (6)$$

where p_0 is the divertor total neutral pressure, c_z is the impurity fraction, f_z is the radiative efficiency of the impurity (18 for nitrogen), λ_q is the heat flux width and r_z is a weak exponent, $r_z < 0.1$, to account for broadening of λ_q in the divertor. As in the empirical scaling of Eq. 5, the neutral pressure required for detachment is proportional to the upstream heat flux density. While there are similarities between this model and the Self-Ewald model of Eq. 4 and the modeling of Refs. [44, 55] the latter have no power dependence with $T_{e,div}$ dependent only on the neutral density. Further analysis and modeling will likely be required to address this discrepancy, though it may be related the global pressure measurement in the ASDEX-Upgrade data compared to the local neutral density at the target for each flux tube. Additional analytic considerations of divertor detachment and dissipation are discussed in the companion paper by Stangeby [23].

The role of atomic physics, and its associated dissipation of energy and momentum, in the detached divertor plasma has also been studied by utilizing helium plasmas instead of hydrogenic species. The use of helium removes molecular processes, reduces the role of charge-exchange momentum loss and simplifies the overall description of radiative losses. Detachment studies in helium plasmas have been reported from JET [82], ASDEX-Upgrade [83] and DIII-D [84]. For helium discharges without auxiliary heating the longer ionization length often results in more core radiation with divertor detachment due to loss of power flowing into the divertor. By the onset of detachment an X-point MARFE has often formed. In DIII-D auxiliary heating with helium neutral beam injection allowed study of detached plasmas with the primary dissipation of energy and momentum occurring within the divertor [84]. In this case fluid modeling with SOLPS was able to reproduce the divertor plasma profiles as well as pressure and heat flux loss as a function of parallel distance from the X-point to the target. This encouraging result suggests that fluid models can capture the appropriate parallel transport physics within the divertor if the atomic physics is modeled correctly. Further comparison of divertor detachment experiments with modeling are presented in the companion paper by Canik and Groth [20].

VI. In/Out divertor asymmetry and plasma drifts

Asymmetries between the inboard and outboard divertor plasma characteristics, including detachment, have long been observed in tokamaks. A typical comparison between inboard and outboard divertor profile in a C-Mod L-mode plasma is shown in the left-hand column of Fig. 12 [46,85,86].

For the standard toroidal field direction, where the ion $\vec{B}\times\vec{\nabla}B$ drift direction is directed from the midplane into the divertor (□B drift ↓), the outboard divertor plasma is at higher temperature and lower density than the inboard divertor plasma. This asymmetry results in much higher heat flux to the outboard divertor target but higher radiated power in the inboard divertor plasma [87-92]. Taking radiated power and surface heat flux together, power accounting in DIII-D indicated that the total power flowing into the outboard divertor is approximately 30% greater than the inboard and remains constant across a range of conditions, including variation of input power and plasma density through detachment [89]. In fact, for H-mode plasmas in low-Z tokamaks without additional gas injection the inboard divertor often displays characteristics of detachment with high radiated power fraction, low electron pressure and spectroscopic signatures of plasma recombination [4,92-94]. This in/out asymmetry of divertor plasmas typically leads to the inboard divertor detaching at a lower core density than the outboard divertor as shown in the example from the JET Mark I divertor in Fig. 13 [4]. In this H-mode density scan the inboard divertor begins to detach between ELMs, Fig. 13b, at a lower lined-averaged density and eventually achieves a much higher degree of detachment (DOD) than the outboard divertor.

While factors such as toroidicity and outboard ballooning transport may contribute, divertor asymmetry is understood to be primarily driven by $\vec{E}\times\vec{B}$ plasma drifts. As described in Ref [95,96] electric fields in the divertor and SOL plasma primarily arise from gradients in the electron temperature profile, □T_e. Therefore, as sketched in Fig. 14a, the poloidal gradient in T_e, from the target towards the midplane, drives a radial $\vec{E}\times\vec{B}$ particle flux in the outboard divertor from the SOL towards the separatrix and into the private flux region. In the inboard divertor the radial $\vec{E}\times\vec{B}$ particle flux has the opposite effect, driving particle flux from the private flux region across the separatrix into the SOL. The radial gradient in T_e, however, drives a poloidal particle flow, carrying particles from the outboard private flux region across to the inboard divertor private flux region. Reversing the toroidal field direction (□B drift ↑) reverses these flows as shown in Fig. 14b. The magnitude of this particle flux from can be quite significant, as evidenced by an insertable Langmuir probe in DIII-D [97] where the total particle flux from the outboard to the inboard divertor was measured at up to 50% of the total ion flux to the outboard target.

The importance of $\vec{E}\times\vec{B}$ flows on divertor asymmetry and particularly divertor detachment have been studied by comparing discharges with reversed toroidal field directions in several tokamaks, including Alcator C-Mod [46,86,98], JT-60U [29,99], JET [4,100,101], and DIII-D [102]. For low density attached divertor conditions, reversing the toroidal direction (□B drift ↑) typically results in more symmetric plasma conditions between the inboard and outboard divertors as shown in Fig. 12 from Alcator C-mod. This, in turn, leads to more symmetric detachment onset for reversed field. Tokamaks have typically reported that reversed field results in nearly symmetric detachment onset between the inboard and outboard divertor at a lower line-averaged density than for outboard divertor detachment in the forward field direction. A consequence of this increased symmetry in reversed field can be a lower density limit. JET has reported reversed field lowers the line-averaged density limit, ~15%, where complete divertor detachment results in an X-point MARFE, degraded core confinement and eventual plasma disruption [4,100].

The symmetry of detachment onset with increasing density is highlighted in Fig. 15 from DIII-D [103]. The peak $T_{e,div}$, measured by Thomson scattering, is plotted for both the inboard and outboard divertor as a function of line-averaged density in ELMing H-mode for both directions of the toroidal field. The data is collected between ELMs. Consistent with the previously listed observations in the standard toroidal field direction (□B drift ↓) the inboard divertor reaches a cold, dense state characteristic of detachment ($T_{e,div} \leq 5$ eV) at a significantly lower line-averaged density than the outboard divertor. With toroidal field reversal (□B drift ↑) the inboard and outboard divertors become nearly symmetric, with peak $T_{e,div}$ and $n_{e,div}$ values between the inboard and outboard values of the □B drift ↓ case.

Interestingly, a DIII-D L-mode density scan with the same divertor configuration produced the opposite effect to that in H-mode with □B drift ↑ causing the outboard divertor to detach at a higher line-averaged density than for □B drift ↓ [104]. A modeling comparison of the H-mode and L-mode density scans was able to explain this difference in terms of the radial and poloidal $\vec{E}\times\vec{B}$ flows. As shown in Fig. 14, the poloidal T_e gradient results in an $\vec{E}\times\vec{B}$ radial particle flux from the outboard divertor SOL towards and across the separatrix. In H-mode the strong radial T_e gradient results in a poloidal $\vec{E}\times\vec{B}$ drift carrying particles just inside the separatrix in the private flux region from the outboard to the inboard divertor. The loss of density in the outboard divertor due to the poloidal drift results in a higher $T_{e,div}$, requiring a high line-averaged density to achieve detachment. In L-mode radial confinement is much poorer resulting in a lower radial gradient in $T_{e,div}$, and thus reduced poloidal flux of particles from outboard to inboard. This allows the radial $\vec{E}\times\vec{B}$ drift to dominate over the poloidal drift for determining particle flux in the outboard divertor. For L-mode this implies the radial particle flux from the outboard SOL to the separatrix increases $n_{e,div}$ and decreases $T_{e,div}$ and thereby promote detachment in the outboard divertor for the □B drift ↓ case compared to the □B drift ↑ case.

Finally the effects of drifts due to field reversal on the 2D profile of divertor T_e and n_e was detailed by divertor Thomson scattering in DIII-D [103]. In Fig. 16 is shown the 2D T_e and n_e profiles for both the inboard and outboard divertors for detached divertor H-mode conditions with both directions of the toroidal field. Again the divertor Thomson data is collected between ELMs in H-mode. Many of the features of detached plasmas are highlighted in these profiles. In Fig. 16, left column, the outboard divertor has just achieved detachment at a line-averaged density of $n/n_{GW}=0.75$, with target separatrix $T_e \leq 5$ eV. Further out in the SOL the target is still attached with $T_e \sim 10$ eV. The asymmetry with the inboard divertor is readily apparent with the detachment front, $T_e < 5$ eV, moving half way up the inboard divertor leg from the target to the x-point. Asymmetry in the density profile is also clearly seen in Fig. 16, lower left figure, where the radial $\vec{E}\times\vec{B}$ drift shifts the density to smaller major radius. The radial drifts result in significant density in the private flux region just inside of the separatrix in the outboard divertor, and a region of very high density in far SOL of the inboard divertor. Other tokamaks have reported similar observations with significant private flux region density observed in Alcator C-mod [105], and high density observations in the far SOL inboard divertor in ASDEX-Upgrade [106]. At a somewhat higher density, $n/n_{GW}=0.79$, the outboard divertor detaches completely with $T_e < 5$ eV and $n_e > 3x10^{20}$ m^{-3} nearly up to the X-point. Below the detachment zone the inboard and outboard divertor conditions are now more symmetric. This is indicative of the low T_e with reduced gradient driving much less $\vec{E}\times\vec{B}$ flows in this region. An ASDEX-Upgrade study also found less divertor asymmetry in regions of low T_e gradient [107].

Detachment in the □B drift ↑ case exhibits greater overall divertor symmetry as shown in Fig. 16 third column. In this case at a somewhat lower line-averaged density of n/n_{GW}= 0.72, the divertor T_e profiles are much more symmetric with the detachment front moving half way up both divertor legs. The density profiles are also more symmetric with both divertor legs achieving similar density levels. The outboard divertor density profile has also shifted to larger major radius compared to the □B drift ↓ case of Fig. 16 center column. The density is reduced in the private flux region of the outboard divertor and the high density extends further out into the SOL.

VII. Transient detachment due to ELMs

While detached plasmas are often studied in L-mode, or ohmic, conditions for the quiescent plasmas they provide, H-mode is more relevant due to the higher power available that will be characteristic of divertor plasmas in DEMO-scaled tokamaks. However, transient ELMs are a ubiquitous feature of standard H-mode operation, where the H-mode transport barrier causes the edge pressure gradient to grow uncontrollably until an MHD limit is exceeded. The resultant instability releases particles and energy into the SOL plasma in a short time, ~100 μsec. A review of ELM characteristics and their consequences can be found in Ref [108]. The evolution of ELM transients released into the SOL, propagation to the divertor and interaction with the divertor plasma has been studied in a number of tokamaks including JET [109], ASDEX-Upgrade [110] and DIII-D [111]. Detached divertor evolution during an ELM pulse is highlighted in Fig. 17 with tangential images of CIII emission in DIII-D [112]. In high density detached plasmas before an ELM the CIII emission, characteristic of the region with $T_{e\sim}$ 5-10 eV, is peaked up the divertor leg near the X-point. During the ELM the plasma reheats pushing the CIII emission to near the target. Only in very small ELM regimes, such as Type II ELMs studied in ASDEX-Upgrade [113], are the ELMs sufficiently buffered by cold dense divertor plasma to avoid reattaching the divertor target with the ELM heat pulse. After the ELM energy dissipates in the divertor, typically a few hundred μsec, the high density remaining in the divertor from the ELM results in the divertor becoming detached again. Even for attached plasmas the additional density of the ELM often leads to temporary divertor detachment after the ELM energy dissipates on a much faster timescale than the density. The high divertor density remaining after the ELM typically dissipates to an equilibrium baseline level ≤ 10 msec after the ELM event. Therefore the analysis of detached divertor H-mode plasmas described in the previous sections is carried out between ELMs, after the divertor plasma has returned to equilibrium from the previous ELM transient. While such ELM-conditional analysis is straightforward when the ELM frequency is relatively low, ≤ 50 Hz, at higher ELM frequency, such as with higher power, the analysis is more problematic with insufficient time for the divertor plasma to return to equilibrium.

In future DEMO-scale tokamaks ELM control will have to be integrated with detached divertor operation to protect the divertor targets from excessive erosion and damage. Detached divertor plasmas alone will be insufficient to buffer the targets from the ELM heat pulse[114]. The constraints ELM control will place on detached divertor plasmas will depend on the specific ELM control techniques employed. A leading concept for ELM control is the use of 3D fields, resonant magnetic perturbations (RMPs), to limit the growth of the pedestal pressure below the MHD limit [115,116]. A summary of the current understanding of the interaction of divertor detachment with 3D fields in divertors and stellerators can be found in the companion paper by Ahn [22]. In existing devices the application of 3D fields does not typically greatly alter the density required for achieving detachment, though 3D structures may remain in the divertor plasma that must be taken into account [117,118]. Another technique for ELM control relies on triggering ELMs at a high frequency, such as through pellet injection, to reduce their amplitude. Not a lot of work has been done examining the interaction of pellet ELM pacing with divertor detachment, but a significant issue will be the consistency of the particle throughput required for ELM control with that required for maintaining divertor detachcment. Finally, naturally ELM–free regimes can be considered for compatibility with detached divertor operation. Unfortunately most ELM-free regimes, such as QH-mode, that appear promising for DEMO-scale tokamaks have yet to be demonstrated in existing devices. A challenge for studying divertor detachment in the presence of such ELM control techniques is that the relevant studies require low collisionality pedestal conditions, while divertor detachment requires high density and collisionality in existing devices. While these techniques may scale towards detached divertor operation in future larger tokamaks, the effect of ELM control, such as increased radial transport, will need to be taken into account.

VIII. Divertor configuration

Divertor configuration has been shown to significantly affect divertor detachment onset and overall characteristics in a number of tokamaks through variations in divertor target and baffle geometry as well as magnetic configuration. An extensive review of the effects of divertor target and baffle geometry on divertor plasmas can be found in Loarte [119]. Only a summary of the major effects on detachment are summarized here. An example of different geometries as examined in Alcator C-Mod is shown in Fig. 18 [46]. Three different geometries as shown were tested in C-Mod, 1) a vertical target with a steep incline with respect to the separatrix (Fig. 18a), 2) a slot divertor with the separatrix on a horizontal plate but the close fitting baffle again with a steep angle with respect to the separatrix (Fig. 18b), and 3) a shorter leg divertor intersecting a more horizontal plate in an open configuration with no close fitting baffle (Fig. 18c). An ohmic density scan exhibited very different detachment characteristics across the three configurations as shown in Fig. 19. In both the slot and vertical plate geometries divertor detachment starts at the separatrix and moves out into the SOL with increasing line-averaged density. Here detachment is defined as a 50% loss of electron pressure from the midplane to the target. For the flat-plate configuration without an incline with respect to the separatrix, Fig. 18c, a much higher line-averaged density is required to achieve divertor detachment.

A similar effect on detachment has been reported in ASDEX-Upgrade with the modification from the open Div-I divertor to the more closed Div-II Lyra divertor, Fig. 20 [120]. Similar to the C-Mod results, in the vertical target, Div-II, configuration the target separatrix achieves detachment, defined as ion flux rollover, at a lower upstream density than for the open horizontal target Div-I configuration. However further out into the SOL, or further up the vertical target, the plasma remains attached. This results in the total ion target flux as a function of midplane separatrix density being similar between the horizontal and vertical target configurations. This behavior is very similar to B2-EIRNE simulations of the configurations as shown in Fig. 21. Further increase of density, or divertor radiation due to seeded impurities, has been able to completely detach the outboard divertor target, but typically results in a radiating MARFE forming in the X-point region with associated pedestal and core confinement degradation [121].

Qualitatively similar results were obtained in JT-60U when they replaced their open divertor with a more closed W-shaped divertor as shown in Fig. 22a [47]. While the JT-60U W-shaped divertor is less closed with a shallower angle with respect to the separatrix than the C-Mod and ASDEX-Upgrade Div-II divertors, many of the same advantages were obtained. As shown in Fig. 22b and 22c, the W-shaped divertor produced a higher n_e and lower T_e near the strikepoint compared to open divertor at the same line-averaged density. This resulted in divertor detachment onset at 10%-20% lower lined averaged density across all ranges of input power, as shown in Fig. 23. A factor of 5 greater electron pressure loss in the W-shaped divertor was also reported. Similar to the C-Mod and ASDEX-Upgrade results the detachment occurred for a relatively narrow region around the separatrix with the plasma further out in the SOL remaining attached until increasing density, or impurity seeding results in an X-point MARFE.

The divertor modifications, and subsequent experimental results, from C-Mod, ASDEX-Upgrade and JT-60U are all consistent with the physical concept of inclining the divertor target with respect to the separatrix to reflect recycling neutrals towards the separatrix. The higher neutral pressure near the strike-point increases n_e, lowers T_e and promotes detachment at the separatrix but inhibits detachment further out in the SOL with lower neutral pressure in that region. This concept can also be considered consistent with the 2D divertor profiles from DIII-D in Fig. 10 where the open and horizontal target of DIII-D allows simultaneous detachment across the divertor target before the detachment front near the separatrix moves up to the X-point. Indeed recent experiments with a more closed upper divertor in DIII-D resulted in divertor detachment at lower line-averaged density [122].

The dependence of target geometry and divertor baffling was further tested by a series of divertor modifications carried out on JET as summarized by Rapp [123]. The effect of divertor closure was examined with the configurations as illustrated in Fig. 24. The open configuration was created by raising the X-point to bring the divertor plasma above the baffle structure as illustrated by the magnetic equilibrium with the dashed red lines. Consistent with the previously noted results, L-mode discharges in this more open divertor required ~15% higher core density to achieve detachment of the outboard divertor, compared to the more closed configuration shown by the black magnetic equilibrium in Fig. 24. Control of neutrals was also tested with removal of the center septum shown in Fig. 24. The septum was designed to limit neutral flux back into the core plasma through the private flux region and to isolate the outboard divertor from the inboard. By comparing discharges with the septum to later discharges after its removal, the septum was found maintain a higher asymmetry between the inboard and outboard divertors. With the septum the inboard divertor density is higher and detaches more easily. While $T_{e,div}$ is generally lower in the outboard divertor with the septum, the density is also lower and detachment is not achieved until just before an X-point MARFE forms. In general the effects of the septum were modest and did not significantly affect the core plasma performance.

The JET divertor also tested the role of the divertor target angle with the Vertical Target (VT) configuration compared to the Horizontal Target (HT) as shown in Fig. 25 [4,28,124,125]. In contrast to the previously presented results, divertor detachment in JET was obtained with similar midplane density profiles in both the VT and HT configurations for ohmic and L-mode discharges. This is despite the fact that a factor of 2 increase in divertor neutral pressure was measured for the VT configuration. For JET H-mode discharges similar results have been observed, as shown in Fig. 26, where at the same line-averaged density the VT configuration exhibited a similar T_e profile at the target as the HT configuration, even though the ion flux was significantly higher near the separatrix. However, modeling (solid lines in Fig. 26) predicts detachment near the separatrix for the VT configuration, similar to the behavior summarized above from C-Mod, ASDEX-Upgrade and JT-60U. Speculations as to the possible causes for the different JET results include, 1) 3D neutral bypass leakage and recirculation patterns, 2) scaling of divertor and main chamber radial transport processes, and 3) SOL fluctuations and intermittency of plasma transport. Overall the JET results suggest a number of aspects of divertor configuration play a role in detachment characteristics, including target geometry, far SOL baffling of recirculating neutrals and divertor neutral leakage. The difficulty in modeling these effects highlights the need for better quantitative models to describe divertor detachment. The status and modeling of divertor detachment is summarized in the companion paper by Canik and Groth [20].

Magnetic geometry also has the potential to affect the onset of divertor detachment and its other characteristics. A significant effort in tokamak divertor research has been dedicated to exploiting divertor magnetic geometry to improve divertor detachment performance. The progress and status of these efforts are summarized in a companion paper by Soukhanovskii [21]. However, variations in divertor magnetic geometry also provide an opportunity to probe the physics and scaling of divertor detachment. A series of experiments in TCV explored detachment onset and detachment front location as functions of divertor leg length ($L_{||}$), poloidal flux expansion and major radius of the strike-point location [126, 127]. As can be seen from the Two-Point Model of Eq. 1 the upstream density for detachment onset, $T_{e,div} \sim 5$ eV, is expected to scale as $n_{e,sep} \propto L_{\|}^{-2/7}$. This dependence was tested in TCV, Fig. 24b, exhibiting detachment onset with target ion flux reduction at lower line-averaged density for greater divertor leg length. DIII-D similarly found that a a 3-fold increase in the divertor leg length from the X-point to target, reduced peak $q_{||}$ by a similar factor, and was accompanied by a ∼30% increase in $n_{e,div}$ and ∼30% reduction in $T_{e,div}$ [128,129].

While the $L_{||}$ dependence results were consistent with expectations other parameter dependences were less so. Poloidal field flux expansion has been argued to potentially decrease density at detachment onset through increased ion-neutral interaction near the target. However, poloidal flux expansion did not acheive significant change in detachment onset in TCV, as shown in Fig. 27a. On the other hand NSTX has reported improved divertor detachment access with high poloidal flux expansion in their outer lower divertor [68,130]. Divertor detachment in NSTX was characterized by a drop in target heat and ion flux, increased radiation and spectroscopic signatures of plasma recombination.

Increase in major radius of the strike-point is also expected to reduce the upstream density at detachment onset through a reduction in target $q_{||}$ due to total magnetic field flux expansion. However TCV did not find any change in detachment onset and extent with a large change in the outer strike-point location as shown in Fig. 28. In this case the detachment front formation and location was identified by the location of strong CIII radiation [126]. Similarly DIII-D found that increase of the strike-point major radius did not have the expected effect of reducing $T_{e,div}$ for a fixed midplane density. However in the DIII-D case the experimental deviation from the simple Two Point Model expectation was attributed to the different neutral recycling patterns associated with varying geometry rather than the effects of parallel plasma transport [128,129].

The magnetic geometry experiments described above represent a valuable database for exploring detachment physics, but they also highlight the need for modeling to isolate and interpret the different physical processes responsible for the observed behavior.

Advanced magnetic geometry configurations have also been proposed to improve divertor performance. For example, moving the strike-point to large major radius, or “Super-X” configuration, has been proposed to reduce $q_{||}$ at the target and improve divertor detachment accessibility at lower density [131]. Double –null plasma configurations offer the advantage of an additional divertor to dissipate heat flux [132]. By reversing the direction of current in one of the poloidal coils a secondary poloidal field null can be added to the divertor. With a secondary null near the strike-point in an “X-divertor” configuration, the large poloidal flux expansion is expected to improve detachment access and stability [133,134]. If the secondary null is moved near the primary X-point, a “Snowflake” configuration results with multiple strike-points and the potential enhanced radial diffusion of heat flux [135]. A review of progress on these concepts can be found in the companion paper by Soukhanovskii [21].

IX. Detachment control and stability

To make use of divertor detachment for heat flux control in future devices the level of detachment must be controlled. Most tokamaks have used a combination of deuterium and impurity injection to raise density and radiation in order to lower $T_{e,div}$ as governed by Eq. 1, to a level where ion-neutral interactions become dominant and detachment ensues. However, density and impurity radiation should not be too high in order to avoid collapse of the divertor plasma into an X-point MARFE and concomitant degradation of pedestal and core performance [24,121]. Along with the actuators of fuel and impurity injection, a real-time measure of the state of the divertor plasma is required for active control of divertor detachment.

On ASDEX-Upgrade control of divertor detachment was initially made through injection of neon to maintain total plasma radiation at a fixed fraction of input power as measured in real-time by vertically viewing bolometer array [6]. Subsequently, the temperature of the divertor target has been assessed in real-time through the measurement of target tile current flowing between the inboard and outboard divertors [136]. In/out asymmetry in $T_{e,div}$, and subsequent sheath potential, between the inboard and outboard divertors was found to drive an SOL current between the two divertors directly related to the differences in $T_{e,div}$. With the inboard divertor typically detached in H-mode with the standard toroidal field direction, an outboard $T_{e,div} \sim 5$ eV is achieved when the tile current is reduced to a sufficiently low value [137]. Since the installation of the all tungsten wall in ASDEX-Upgrade the tile current signal has been used to control the level of nitrogen injection and divertor radiation. This heat flux control system has been extended to include control of argon injection for core plasma radiation as measured by a bolometer array [138]. As shown in Figure 29 this system has maintained tolerable peak divertor heat flux below 5 $\mathrm{MWm^{-2}}$ for high power density discharges, $P_{heat}/R = 15\ \mathrm{MWm^{-1}}$, about 2/3 of that expected in ITER, while maintaining good core confinement [34].

Initial work with feedback control of nitrogen injection for divertor detachment on C-Mod utilized a single bolometer channel measuring radiation in the plasma edge near the separatrix [14,27]. This system was able to maintain good confinement and overall performance in an EDA [139] H-mode discharge. Use of feed-forward nitrogen injection typically resulted in excessive radiation and a transition back to L-mode. More recently, as shown in Fig. 30, a real-time system that measured divertor target heat flux with surface thermocouples was able to reduce unmitigated heat flux of >30 MW/m^2 to ~10 MW/m^2 through controlled nitrogen injection while maintaining good H-mode confinement with H_{98}~1.05 [140]. The recent C-Mod results also highlighted the challenge of transient response that may face control of divertor detachment in future reactor scale devices. For C-Mod the timescale of transients due to eroded material or exhaust power is characteristic of the parallel confinement time in the SOL, typically a few milliseconds. However the response time of the nitrogen injector actuator, roughly the distance of the gas valve from the divertor divided by the gas sound speed is much longer at more than 100 milliseconds. A narrow operational window, as observed in the Alcator C-Mod experiments, with too much radiation leading to an X-point MARFE, and too little re-attaching the divertor with significantly greater heat flux, makes the challenge even greater.

Divertor detachment control on DIII-D has also revealed issues related to detachment front stability. Early control of detachment in DIII-D relied on measurement of the midplane neutral pressure [24]. More recent control efforts have made use of a divertor Thomson scattering diagnostic to directly measure $T_{e,div}$ just above the target [141]. In DIII-D detachment control is provided by deuterium gas injection to raise the divertor density and radiation from the intrinsic carbon impurity. The Thomson scattering makes a fast $T_{e,div}$ measurement every 20 msec at a location about 1 cm above the target. In H-mode ELM effects lasting roughly 5 msec are detected by a divertor Dα signal and filtered from the Thomson measurements. When requesting a $T_{e,div}$ of 5 eV, the divertor plasma was found to oscillate between conditions with $T_e > 10$ eV and $T_e \leq 2$ eV. This bifurcation of divertor states is consistent with other DIII-D measurements of divertor T_e as a function of upstream plasma density [50]. As shown in Fig. 31, with increasing midplane separatrix density the outer strike-point $T_{e,div}$ decreases until it reaches a "cliff" at ~10 eV where it rapidly transitions to $T_e \leq 2$ eV. The $T_{e,div}$ cliff is more pronounced at higher input power and barely distinguishable in low-power L-mode. The rapid transition is not universal however, as shown by the ASDEX-Upgrade example of Fig. 29 where $T_{e,div}$ was smoothly reduced to ~ 5eV with nitrogen injection. The rapid transition in $T_{e,div}$ in DIII-D has been qualitatively explained in terms of the cross-field drifts described in Section VI, but further work is required before predictive capability of this behavior in future devices is available.

Other indications of detachment instability have been seen in the 2D profiles of detached divertor plasmas in DIII-D. Shown in Fig. 32a is the 2D profile of T_e in a DIII-D detached H-mode plasma as reconstructed from Thomson scattering measurements. In Fig. 32b the relative standard deviation of the temperature measurements are shown. While above and below the detachment zone, $T_e \geq 12$ eV and $T_e \leq 5$ eV respectively, the measurements are relatively constant and stable, in the detachment zone, 5 eV $\leq T_e \leq$ 12 eV, the fluctuations are large. Due to the periodic sampling of the Thomson scattering, one measurement every 20 ms, it is not possible to discern the frequency or the spatial scale of the turbulence. The DIII-D fluctuations are suggestive of fluctuating detachment measurements in the inboard divertor of ASDEX-Upgrade [142], though it is not yet clear how, or if they are related. Also the detachment turbulence may, or may not be related to the divertor state bifurcations discussed earlier. Whichever the case, detachment stability is clearly worthy of further work due to its implications for detachment control in future tokamaks.

X. Detachment effects on core confinement and performance

Besides providing for divertor heat flux and target plate erosion control, divertor detachment must be made compatible with high confinement and overall performance of the core plasma in future tokamaks. In low-Z tokamaks with only deuterium injection, degradation of normalized core confinement can usually be limited to a modest level of 10% to 15%, if the gas injection only achieves partial detachment of the outboard divertor [8,9]. If the density is raised further with additional deuterium injection for more complete detachment across the divertor target typically the highly radiative region moves upstream and into the closed field lines near the X-point. This X-point MARFE resulted in significantly larger drop in core confinement, or even a transition back to L-mode. The response of the normalized confinement "H-factor" to increase in density in JT-60U [47], as shown in Fig. 33, is qualitatively typical of the response to additional deuterium injection in most Low-Z tokamaks.

More complete detachment with better core confinement has often been obtained by injecting impurities to enhance radiative losses. The motivation for this technique can be seen in Eq. 1 where higher levels of radiated power, f_{pow}, should result in detachment at a lower upstream density, n_{sep}, more compatible with high core confinement. Early experiments in ASDEX-Upgrade made use of neon injection, along with deuterium, to obtain complete divertor detachment while still maintaining high core confinement [7]. Similar high core confinement results with impurity injection have also been obtained DIII-D [143,144] and JT-60U [145,146]. In metal-wall tokamaks deuterium, with low intrinsic impurity radiation, deuterium injection alone into H-mode typically results in a transition back to L-mode before divertor detachment is obtained. In C-Mod [27], the all-tungsten ASDEX-Upgrade [31,138] and the ITER-like wall JET [147,148] have all obtained divertor detachment with good core confinement with impurity injection.

In order to project the compatibility of divertor detachment with good core performance towards future devices, it is important to understand the physical processes leading to confinement degradation in existing experiments. In H-mode the most direct effect of divertor detachment on core confinement is through the edge pedestal. In DIII-D any degradation of the edge pedestal with increases in density and outboard divertor detachment was found consistent with edge MHD stability as shown in Fig. 34 [149]. Divertor detachment in low-Z tokamaks with deuterium injection usually leads to higher pedestal density and collisionality. The higher pedestal collisionality suppresses the edge bootstrap current resulting in a lower MHD stability limit, particularly for strongly shaped plasmas [150,151]. In addition, in ASDEX-Upgrade higher density was found to lead to a steeper pressure gradient just inside of the separatrix resulting in an overall lower pedestal MHD pressure limit [152].

In future larger tokamaks the effects of detachment on pedestal performance may be significantly less than in existing devices. In larger-scale future devices reduced neutral fueling of the pedestal from edge recycling and size scaling of the pedestal is expected to lead to a low collisionality pedestal even for detached divertor conditions [153]. However, an accurate prediction of midplane separatrix density for detached divertor conditions will be required to more fully develop divertor solutions compatible with future device scenarios. In DIII-D, a study of separatrix density just before onset of divertor detachment found general agreement with the Two-Point Model of Eq. 1, as long as energy and momentum dissipation, f_{pow} and f_{mom} are taken into account [154]. Further work on understanding the scaling of separatrix density with detached divertor plasmas as well as pedestal density transport is needed to accurately predict the compatibility of detached divertor operation with high pedestal pressure in future devices.

Limits to impurity injection for enhancing divertor detachment are also typically due to degradation of core performance. A fraction of impurities seeded for increased divertor and SOL radiation will be transported to the core plasma. In addition to dilution of main ion species that would cause reduction of fusion performance in a reactor, additional core radiation from impurities can also degrade core confinement. While additional radiation from the pedestal region inside the separatrix can aid divertor detachment by reducing the SOL heat flux, if it is excessive it can degrade the pedestal. Studies of impurity injection on C-Mod [155] and DIII-D [156] have found that increasing core radiation can reduce H-mode pedestal pressure and core confinement if the power flowing across the separatrix is reduced to near that required for attaining H-mode, P_{LH}.
Some mitigation of pedestal degradation due to high core radiation may be possible with core profile peaking effects . In ASDEX-Upgrade strong nitrogen injection was able to completely detach both divertor targets and resulted in strong stable radiation localized to the X-point region. While the large X-point radiative losses resulted in a decrease of pedestal top pressure of about 60%, increased gradients inside of the pedestal top resulted in only about a 10% drop in plasma pressure inside of $\rho < 0.7$ [96]. Core confinement improvement with impurity injection has also been observed in DIII-D [143] and is usually a result of additional peaking of the pressure profile. The physical processes leading to confinement improvement with impurity injection is not well understood. Therefore more work is needed to determine how impurity injection for divertor detachment in future tokamaks will affect overall performance.

Divertor detachment also has the potential to directly degrade the H-mode pedestal through additional turbulence. At high density a broad SOL density with enhanced filamentary radial transport is typically observed. With increasing density the filamentary transport originates closer to the separatrix eventually leading to enhanced radial transport across the separatrix. A multi-machine study has found that broad SOL density gradients, and its associated transport, is strongly correlated with high collisionality in the divertor where the SOL magnetic field lines meet the material surface [152]. The SOL density scale length, λ_n, as a function of normalized divertor collisionality, Λ_{div}, in ASDEX-Upgrade, JET and COMPASS is shown in Fig. 35. The high collisionality is thought to interrupt the return of curvature polarization currents and leads to radial filamentary propagation. The correlation of a broad λ_n and filamentary transport at the midplane separatrix with divertor strikepoint detachment in H-mode is less well established. If this correlation holds in H-mode this process may represent a significant limitation for divertor detachment and heat flux control in future tokamaks.

XI. Summary

This report has summarized empirical observations of divertor detachment in tokamaks with low-Z walls. Detachment of the divertor target from the upstream midplane plasma has been achieved in terms of energy, momentum and particle flux dissipation. In tokamaks with low-Z walls, energy dissipation is provided primarily by radiation from the intrinsic wall material impurity, typically carbon, in the T_e range of 5 - 15 eV. Momentum loss occurs for $T_e < 5$ eV where ion-neutral elastic collisions and charge-exchange processes begin to dominate over ionization. Finally for $T_e \leq 1$ eV plasma recombination can result in a significant loss of particle flux. In tokamaks at high power density these processes are often coupled together. Once density is raised and $T_{e,div}$ drops to where low-Z impurity radiation becomes efficient, copious radiative power further lowers $T_{e,div}$ to where hydrogenic radiation and neutral effects become dominant. This in turn further lowers $T_{e,div}$ to where significant recombination can occur. This coupling of processes leads to a rapid transition from attached divertor plasmas to detached conditions with significant losses in energy, momentum and particle flux for only a modest increase in upstream plasma density. Different tokamaks in the international fusion community employ different diagnostics to monitor divertor detachment, usually emphasizing one of the loss channels, energy, momentum, or particle flux due to recombination. In practical terms divertor detachment usually involves significant levels of loss in all three channels.

In order to predict divertor detachment behavior, and the conditions required to achieve it in future tokamaks, the influence of different configurations and processes has been examined. Plasma $\vec{E}\times\vec{B}$ drifts arising from gradients in T_e are observed to have significant influence on detachment onset and its resulting spatial symmetry. Divertor configuration, both the baffling structure and magnetic configuration, can also significantly affect detachment characteristics, primarily through its effect on the neutral plasma interaction. Observations of detachment front control, instability and turbulence have been documented. Finally the interaction of divertor detachment with core confinement and overall performance has been examined with the interaction primarily mitigated through the H-mode edge pedestal.

To fully predict and optimize divertor detachment required for heat flux control in future tokamaks, a validated model of the SOL, divertor and pedestal under detached conditions is required. The progress in development of such models is presented in a companion paper. The data obtained by the international fusion development effort summarized in this report should serve as a useful database for the development and testing of these models.

Acknowledgement

The author wishes to thank Dan Thomas, Adam McLean, Aaro Jaervinen, Peter Stangeby, and David Hill for helpful discussions in compiling this review. This material is based upon work supported by the U.S. Department of Energy, Office of Science, Office of Fusion Energy Sciences, using the DIII-D National Fusion Facility, a DOE Office of Science user facility, under Awards DE-FC02-04ER54698. DIII-D data shown in this paper can be obtained in digital format by following the links at **https://fusion.gat.com/global/D3D_DMP**

References

[1] Janeschitz G, Borrass K, Federici G and Igitkhanov Y 1995 *J. Nucl. Mat.* **220-222** 73

[2] Najmabadi F, Abdou A, Bromberg L *et al* 2006 *Fusion Engineering and Design* **80** 3

[3] Tobita K, Nishio S, Sato M, *et al* 2007 *Nucl. Fusion* **47** 892

[4] Loarte A, Monk R D, Martin-Solis J R, 1998 *Nucl. Fusion* **38** 331

[5] Gruber O, Kallenbach A, Kaufmann M *et al* 1995 *Phys. Rev. Lett.* **74** 4217

[6] Kallenbach A, Dux R, Mertens V and Gruber O 1995 *Nucl. Fusion* **35** 1231

[7] Neuhauser J, Alexander M, Becker G *et al* 1995 *Plasma Phys. Control. Fusion* **37** A37

[8] Petrie T W, Buchenauer D, Hill D N and Klepper C 1992 *J. Nucl. Mater.* **196-198** 848

[9] Petrie T W, Hill D N, Allen S L *et al* 1997 *Nucl. Fusion* **37** 321

[10] Allen S L, Brooks N H, Bastasz R, *et al* 1999 *Nucl. Fusion* **39** 2015

[11] Leonard A W 2005 *Fusion Science and Technology **48** 1083*

[12] Hosogane N, Asakura N, Kubo H and Itami K 1992 *J. Nucl. Mater.* **196-198** 750

[13] Lipschultz B, Goetz J and LaBombard B 1995 *J. Nucl. Mater.* **220-222** 50

[14] Goetz J A, Lipschultz B, Graf M A and Kurz C 1995 *J. Nucl. Mater.* **220-222** 971

[15] Goetz J A, Kurz C, LaBombard B and Lipschultz B 1996 *Phys. Plasmas* **3** 1908

[16] Matthews G F 1995 *J. Nucl. Mater.* **220-222** 104

[17] Borrass K and Janeschitz G 1994 *Nucl. Fusion* **34** 1203

[18] Stangeby P C 1993 *Nucl. Fusion* **33** 1695

[19] Stangeby P C 2000 *The Plasma Boundary of Magnetic Fusion Devices* (Bristol:IOP Publishing)

[20] Canik JM and Groth M submitted to *Plasma Phys. Control. Fusion*

[21] Soukhanovskii V A 2017 *Plasma Phys. Control. Fusion* **59** 064005

[22] Ahn J-W, Briesemeister A R, Kobayashi M *et al* 2017 *Plasma Phys. Control. Fusion* **59** 084002

[23] Stangeby P C submitted to *Plasma Phys. Control. Fusion*

[24] Petrie T W, Maingi R, Allen S L *et al* 1997 *Nucl. Fusion* **37** 643

[25] Allen S L, Brooks N H and Campbell R B 1995 *J. Nucl. Mater.* **220-222** 336

[26] Fenstermacher M E, Wood R D and Allen S L 1997 *J. Nucl. Mater.* **241-243** 666

[27] Goetz J A, LaBombard B, Lipschultz B *et al* 1999 *Phys. Plasmas* **6** 1899

[28] Matthews G F 1995 *Plasma Phys. Control. Fusion* **37** A227

[29] Asakura N, Hosogane H, Tsuji-Iio S *et al* 1996 *Nucl. Fusion* **36** 795

[30] Fenstermacher M E, Allen S L and Brooks N H 1997 *Phys. Plasmas* **4** 1761

[31] Kallenbach A, Bernert M, Beurskens M, *et al* 2015 *Nucl. Fusion* **55** 053026

[32] Kubo H, Sugie T, Shimada M and Hosogane N 1993 *Nucl. Fusion* **33** 1427

[33] Kubo H, Sugie T, Hosogane N *et al* 1995 *Plasma Phys. Control. Fusion* **37**

1133

[34] Kallenbach A, Kaufmann M, Coster D P *et al* 1999 *Nucl. Fusion* **39** 901

[35] Wenzel U, Carlson A, Fuchs C *et al* 1999 *Plasma Phys. Control. Fusion* **41** 801

[36] Wenzel U, Thoma A, Dux R and Fuchs C 1997 *J. Nucl. Mater.* **241-243** 728

[37] Isler R C, Wood R W and Klepper C C 1997 *Phys. Plasmas* **4** 355

[38] Allen S L, Hill D N, Carlstrom T N and Nilson D G 1997 *J. Nucl. Mater.* **241-243** 595

[39] Isler R C, Colchin R J, Brooks N H and Evans T E 2003 *J. Nucl. Mater.* **313-316** 873

[40] Brooks N H, Isler R C and McLean A G 2007 *J. Nucl. Mater.* **363-365** 131

[41] Roth J 1999 *J. Nucl. Mater.* **266-269** 51

[42] Whyte D G, Bastasz R, Brooks J N *et al* 1999 *J. Nucl. Mater.* **266-269** 67

[43] Groth M, Brezinsek S, Belo P *et al* 2013 *Nucl. Fusion* **53** 093016

[44] Jaervinen A E, Giroud C, Groth M *et al* 2016 *Nucl. Fusion* **56** 046012

[45] LaBombard B, Goetz J and Kurz C 1995 *Phys. Plasmas* **2** 2242

[46] Lipschultz B, LaBombard B, Terry J L *et al* 2007 *Fusion Science and Technology* **51** 369

[47] Asakura N, Hosogane N, Itami K and Sakasai A 1999 *J. Nucl. Mater.* **266-269** 182

[48] Asakura N, Koide Y, Itami K and Hosogane N 1997 *J. Nucl. Mater.* **241-243** 559

[49] Petrie T W, Allen S L, Carlstrom T N and Hill D N 1997 *J. Nucl. Mater.* **241-243** 639

[50] McLean A G, Leonard A W, Makowski M A *et al* 2015 *J. Nucl. Mater.* **463** 533

[51] Paradela Perez I "SOL parallel momentum loss in ASDEX Upgrade and comparison with SOLPS" 2017 *Nuclear Materials and Energy,* http://dx.doi.org/10.1016/j.nme.2017.01.026

[52] Pitcher C S, Goetz J A and LaBombard B 1999 *J. Nucl. Mater.* **266-269** 1009

[53] Self S A and Ewald H N 1966 *Phys. Fluids* **9** 2486

[54] Wischmeier M, Groth M, Kallenbach A *et al* 2009 *J. Nucl. Mater.* **390-391** 250

[55] Stangeby P C and Sang CF 2017 *Nucl. Fusion* **57** 056007

[56] Kurz C, LaBombard B, Lipschultz *et al* 1997 *Plasma Phys. Control. Fusion* **39** 963

[57] Kocan M, Gunn J P, Carpentier-Chouchana S *et al* 2011 *J. Nucl. Mater.* **415** S1133

[58] Schaffer M J, Bray B D, Boedo J A *et al* 2001 *Phys. Plasmas* **8** 2118

[59] Churchill R M, Canik J M and Chang C S 2016 *et al Nucl. Fusion* **57** 046029

[60] Lumma D, Terry J L and Lipschultz B 1997 *Phys. Plasmas* **4** 2555

[61] Isler R C, McKee G R, Brooks N H *et al* 1997 *Phys. Plasmas* **4** 2989

[62] Fujimoto K, Nakano T, Kubo H *et al* 2009 *Plasma and Fusion Research* **4** 025

[63] Kubo H, Takenaga H, Sawada K *et al* 2005 *J. Nucl. Mater.* **337-339** 161

[64] Wenzel U, Behringer K, Carlson A *et al* 1999 *Nucl. Fusion* **39** 873

[65] Wenzel U, Behringer K, Büchl K and Herrmann A *et al* 1999 *J. Nucl. Mater.* **266-269** 1252

[66] McCracken G M, Stamp M F, Monk R D *et al* 1998 *Nucl. Fusion* **38** 619

[67] Borrass K, Coster D, Reiter D and Schneider R 1997 *J. Nucl. Mater.* **241-243** 250

[68] Soukhanovskii V A, Maingi R, Gates D A *et al* 2009 *Phys. Plasmas* **16** 022501

[69] Krasheninnikov S I, Pigarov A Y and Knoll D A 1997 *Phys. Plasmas* **4** 1638

[70] Terry J L, Lipschultz B, Pigarov A Y *et al* 1998 *Phys. Plasmas* **5** 1759

[71] Lipschultz B, Terry J L, Boswell C *et al* 1999 *Phys. Plasmas* **6** 1907

[72] Leonard A W, Mahdavi M A, Allen S L and Brooks N H 1997 *Phys. Rev. Lett.* **78** 4769

[73] Leonard A W, Mahdavi M A, Lasnier C J *et al* 2012 *Nucl. Fusion* **52** 063015

[74] Asakura N, Sakurai S, Itami K and Naito O 2003 *J. Nucl. Mater.* **313-316** 820

[75] Tsois N, Dorn C, Kyriakakis G and Markoulaki M 1999 *J. Nucl. Mater.* **266-269** 1230

[76] Boedo J A, Porter G D, Schaffer M J and Lehmer R 1998 *Phys. Plasmas* **5** 4305

[77] Boedo J A, Lehmer R, Moyer R A and Watkins J G 1999 *J. Nucl. Mater.* **266-269** 783

[78] Isler R C, Brooks N H, West W P and Leonard A W 1999 *Phys. Plasmas* **6** 541

[79] Post D, Abdallah J and Clark R 1995 *Phys. Plasmas* **2** 2328

[80] Hutchinson I H 1994 *Nucl. Fusion* **34** 1337–48

[81] Kallenbach A, Bernert M, Dux R *et al* 2016 *Plasma Phys. Control. Fusion* **58** 045013

[82] Pitts R A, Andrew P, Andrew Y *et al* 2003 *J. Nucl. Mater.* **313-316** 777

[83] Wischmeier M, Groth M, Wiesen S *et al* 2011 *J. Nucl. Mater.* **415** S523

[84] Canik J M, Briesemeister A R, McLean A G *et al* 2017 *Phys. Plasmas* **24** 056116

[85] LaBombard B, Goetz J A and Hutchinson I 1997 *J. Nucl. Mater.* **241-243** 149

[86] Hutchinson I H, LaBombard B and Goetz J A 1995 *Plasma Phys. Control. Fusion* **37** 1389

[87] Herrmann A, Junker W and Günther K 1995 *Plasma Phys. Control. Fusion* **37** 17

[88] Neuhauser J, Bosch H-S, Coster D *et al* 2003 *Fusion Science and Technology* **44** 659

[89] Leonard A W, Lasnier C J and Cuthbertson J W 1995 *J. Nucl. Mater.* **220-222** 325

[90] Fundamenski W, Pitts R A, Matthews G F *et al* 2005 *Nucl. Fusion* **45** 950

[91] Itami K, Hosogane N, Asakura N and Kubo H 1995 *J. Nucl. Mater.* **220-222** 203

[92] Asakura N, Shimada M, Itami K and Hosogane N 1992 *J. Nucl. Mater.* **196-**

198 1069

[93] Fenstermacher M E, Petrie T W and West W P 1999 *J. Nucl. Mater.* **266-269** 348

[94] Fenstermacher M E, Boedo J, Isler R C *et al* 1999 *Plasma Phys. Control. Fusion* **41** A345

[95] Chankin A V 1997 *J. Nucl. Mater.* **241-243** 199

[96] Chankin A V, Corrigan G, Groth M *et al* 2015 *Plasma Phys. Control. Fusion* **57** 095002

[97] Boedo J A, Schaffer M J, Maingi R and Lasnier C J 2000 *Phys. Plasmas* **4** 1075

[98] Hutchinson I H, Goetz J A and Jablonski D F 1996 *Plasma Phys. Control. Fusion* **38** A301

[99] Asakura N, Itami K, Hosogane N and Tsuji S 1995 *J. Nucl. Mater.* **220-222** 395

[100] Huber A, Rapp J, Andrew P *et al* 2005 *J. Nucl. Mater.* **337-339** 241

[101] Pitts R A, Andrew P, Bonnin X *et al* 2005 *J. Nucl. Mater.* **337-339** 146

[102] Petrie T W, Watkins J G, Baylor L R and Brooks N H 2003 *J. Nucl. Mater.* **313-316** 834

[103] McLean A G, Allen S L, Boedo J *et al* 2017 "*Drift-driven divertor asymmetries in the transition from attached to fully detached conditions*" submitted to *Phys. Plasmas*

[104] Jaervinen A E, Allen S L, Groth M *et al* 2016 "*Investigations of the impact of cross-field drifts on divertor detachment in DIII-D with UEDGE*" Proc. of the 36 EPS conf. on fusion energy

[105] Boswell C J, Terry J L, LaBombard B and Lipschultz B 2001 *J. Nucl. Mater.* **290-293** 556

[106] Potzel S, Wischmeier M, Bernert M *et al* 2015 *J. Nucl. Mater.* **463** 541

[107] Potzel S, Wischmeier M, Bernert M *et al* 2013 *Nucl. Fusion* **54** 013001

[108] Leonard A W 2014 *Phys. Plasmas* **21** 090501

[109] Pitts R A, Andrew P, Arnoux G *et al* 2007 *Nucl. Fusion* **47** 1437

[110] Eich T, Herrmann A, Pautasso *et al* 2005 *J. Nucl. Mater.* **337-339** 669

[111] Leonard A W, Osborne T H, Fenstermacher M E *et al* 2003 *Phys. Plasmas* **10** 1765

[112] Fenstermacher M E, Leonard A W, Snyder P B *et al* 2003 *Plasma Phys. Control. Fusion* **45** 1597

[113] Stober J, Maraschek M, Conway G D *et al* 2001 *Nucl. Fusion* **41** 1123

[114] Loarte A 1997 *J. Nucl. Mater.* **241-243** 118

[115] Evans T E, Fenstermacher M E, Moyer R A *et al* 2008 *Nucl. Fusion* **48** 024002

[116] Snyder P B, Osborne T H, Burrell K H 2014 *Phys. Plasmas* **19** 056115

[117] Briesemeister A R, Ahn J-W, Canik J M *et al* 2017 *Nucl. Fusion* **57** 076038

[118] Brida D, Lunt T, Wischmeier M *et al* 2017 *Nucl. Fusion* **57** 116006

[119] Loarte A 2001 *Plasma Phys. Control. Fusion* **43** R183

[120] Schneider R, Bosch H S, Coster D and Fuchs J C 1999 *J. Nucl. Mater.* **266-269** 175

[121] Reimold F, Wischmeier M, Bernert M *et al* 2015 *Nucl. Fusion* **55** 033004

[122] Wang H Q, *et al* 2016 "*Effect of divertor closure on pedestal fueling and divertor detachment onset in DIII-D"* submitted to *Nuclear Fusion*

[123] Rapp J, Fundamenski W, Ingesson L C *et al* 2008 *Plasma Phys. Control. Fusion* **50** 095015

[124] Jaervinen A E, Brezinsek S, Giroud C *et al* 2016 *Plasma Phys. Control. Fusion* **58** 045011

[125] Groth M, Brezinsek S, Belo P *et al* 2015 *J. Nucl. Mater.* **463** 471

[126] Reimerdes H, Harrison J, Innocente P *et al* 2016 *Proc. Of the 26th Int. Conf. on Fusion Energy* (Kyoto, Japan 17-22 Oct. 2016) EX/2-3

[127] Theiler C, Lipschultz B, Harrison J *et al* 2017 *Nucl. Fusion* **57** 072008

[128] Petrie T W, Canik J M, Lasnier C J and Leonard A W 2013 *Nucl. Fusion* **53** 113024

[129] Petrie T W, Canik J M, Lasnier C J *et al* 2013 *J. Nucl. Mater.* **438** S166

[130] Soukhanovskii V A, Maingi R, Gates D A *et al* 2009 *Nucl. Fusion* **49** 095025

[131] Kotschenreuther M, Valanju P, Mahajan S *et al* 2010 *Nucl. Fusion* **50** 035003

[132] Petrie T W, Brooks N H, Fenstermacher M E *et al* 2008 *Nucl. Fusion* **48** 045010

[133] Kotschenreuther M, Valanju P, Covele B *et al* 2013 *Phys. Plasmas* **20** 102507

[134] Covele B, Kotschenreuther M, Mahajan S *et al* 2017 *Nucl. Fusion* **57** 086017

[135] Soukhanovskii V A, Ahn J-W, Bell R E *et al* 2011 *Nucl. Fusion* **51** 012001

[136] Kallenbach A, Carlson A, Pautasso G and Peeters A 2001 *J. Nucl. Mater.* **290-293** 639

[137] Kallenbach A, Dux R, Fuchs J C *et al* 2010 *Plasma Phys. Control. Fusion* **52** 055002

[138] Kallenbach A, Bernert M, Eich T *et al* 2012 *Nucl. Fusion* **52** 122003

[139] Takase Y, Boivin R L, Bombarda F and Bonoli P T 1997 *Phys. Plasmas* **4** 1647

[140] Brunner D, Wolfe S M, LaBombard B *et al* 2017 *Nucl. Fusion* **57** 086030

[141] Eldon D, Kolemen E, Barton J L *et al* 2016 2017 *Nucl. Fusion* **57** 066039

[142] Potzel S, Wischmeier M, Bernert M *et al* 2013 *J. Nucl. Mater.* **438** S285

[143] Jackson G L, Murakami M, McKee G R *et al* 2002 *Nucl. Fusion* **42** 28

[144] Petrie T W, Wade M R, Brooks N H *et al* 2007 *J. Nucl. Mater.* **363-365** 416

[145] Kubo H, Sakurai S, Asakura N *et al* 2001 *Nucl. Fusion* **41** 227

[146] Asakura N, Nakano T, Oyama N *et al* 2009 *Nucl. Fusion* **49** 115010

[147] Maddison G P, Giroud C, Alper B *et al* 2014 *Nucl. Fusion* **54** 073016

[148] Jaervinen A E, Groth M, Airila M *et al* 2015 *J. Nucl. Mater.* **463** 135

[149] Leonard A W, Makowski M A, McLean A G *et al* 2015 *J. Nucl. Mater.* **463** 519

[150] Snyder P B, Wilson H R, Ferron J R and Lao L L 2004 *Nucl. Fusion* **44** 320

[151] Snyder P B, Aiba N, Beurskens M *et al* 2009 *Nucl. Fusion* **49** 085035

[152] Dunne M G, Frassinetti L, Beurskens M N A M *et al* 2017 *Nucl. Fusion* **59**

025010

[153] Kukushkin A S, Pacher H D, Pacher G W *et al* 2013 *J. Nucl. Mater.* **438** S203

[154] Leonard A W, McLean A G, Makowski M A and Stangeby P C 2017 *Nucl. Fusion* **57** 086033

[155] Loarte A, Hughes J W, Reinke M L, *et al* 2011 Phys. Plasmas **18** 056105

[156] Wang H Q, Guo H Y, Petrie T W, *et al* 2016 "Effect of low-Z and high-Z impurities on divertor detachment and plasma confinement" 2017 *Nuclear Materials and Energy* http://dx.doi.org/10.1016/j.nme.2017.01.027

[157] Carralero D, Siccinio M, Komm M *et al* 2017 *Nucl. Fusion* **57** 056044

Figures

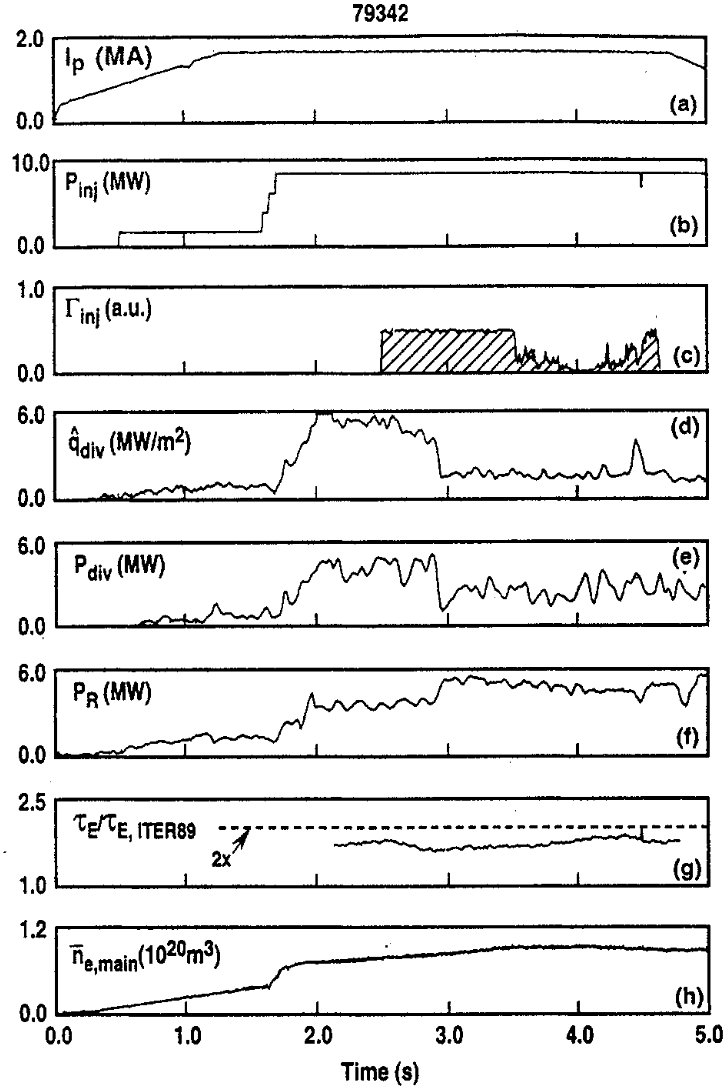

Figure 1. Global behavior of a representative detached divertor discharge in DIII-D H-mode is shown with I_p=1.6 MA, B_t=2.1T, q_{95}=3.7 and injected power P_{inj}= 8.8 MW. Deuterium particle injection was initiated at 2.5 s. The sudden reductions in both peak heat flux (q_{div}) and integrated heat flux (P_{div}) on the divertor tiles at T=2.93 s were coincident with an increase in the total radiated power (P_R). The plasma energy confinement time ($\tau_E/\tau_{E,ITER89}$) normalized to the ITER L-mode energy confinement scaling, and the line-averaged density of the main plasma ($n_{e,main}$) are also shown. [Reprinted courtesy of Reference [9].]

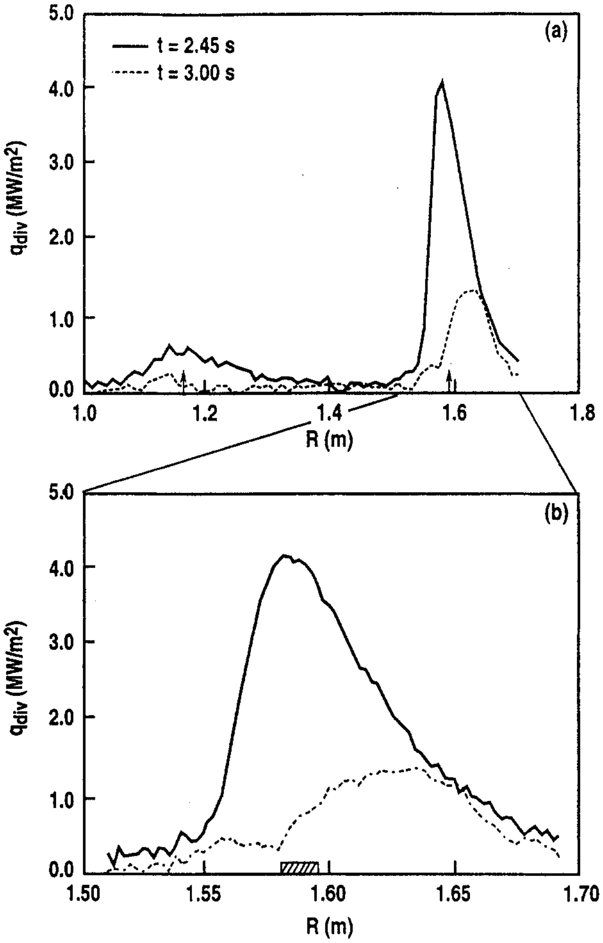

Figure 2. Heat flux across the divertor floor as a function of major radius (R) at two times: (i) pre-puff (t=2.45s in Fig. 1) with the solid line and 0.5 s after deuterium injection (t=3.0 s in Fig. 1) with the dashed line. The arrows in (a) represent the inboard and outboard separatrix strike-points determined from magnetic equilibrium construction. (b) An expanded view of the heat flux profile in the outboard divertor. The shaded area represents the approximate strike-point locations. [Reprinted courtesy of Reference [9].]

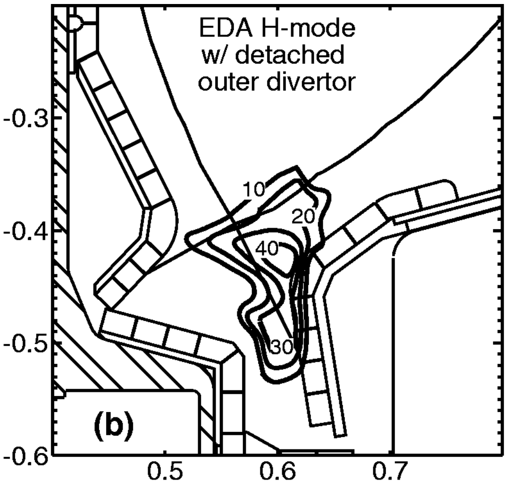
EDA H-mode
w/ detached
outer divertor
10
20
40
30
(b)
-0.3
-0.4
-0.5
-0.6
0.5
0.6
0.7

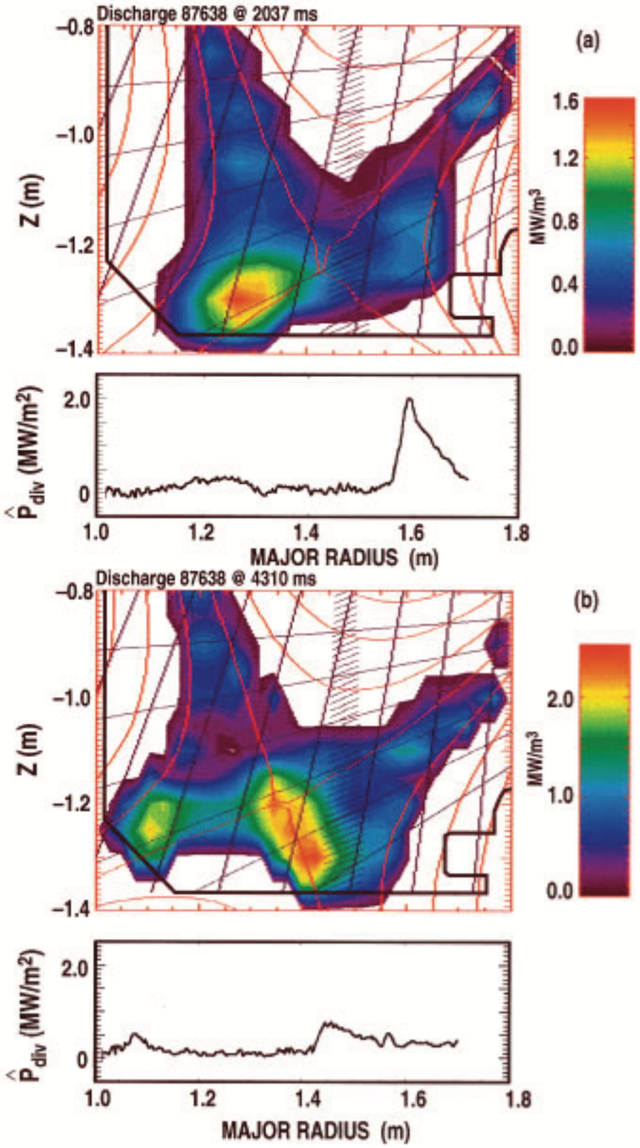
Discharge 87638 @ 2037 ms
(a)
Z (m)
−0.8
−1.0
−1.2
−1.4
MW/m^3
1.6
1.2
0.8
0.4
0.0
$\hat{P}_{div}$ (MW/m^2)
2.0
0
1.0
1.2
1.4
1.6
1.8
MAJOR RADIUS (m)
Discharge 87638 @ 4310 ms
(b)
Z (m)
−0.8
−1.0
−1.2
−1.4
MW/m^3
2.0
1.0
0.0
$\hat{P}_{div}$ (MW/m^2)
2.0
0
1.0
1.2
1.4
1.6
1.8
MAJOR RADIUS (m)

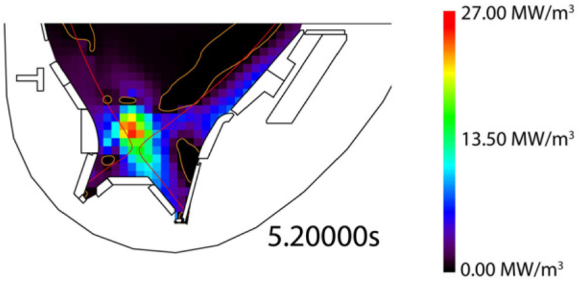

Figure 3. (a) The volumetric emissivity in the divertor region of Alcator C-Mod obtained from bolometer measurements. The emissivity contours are from an EDA H-mode detached outer divertor initiated by nitrogen injection. [Reprinted courtesy of Reference [27].] (b) Reconstructed 2D profiles in DIII-D of radiated power (P_{rad}) from the bolometers arrays and the corresponding heat flux profiles at the target plates during ELMing H-mode and deuterium induced phase of detached radiative divertor. Note the substantial increase of P_{rad} in the outer leg and the corresponding decrease in the peak heat flux at the outboard strike-point. [Reprinted courtesy of Reference [30]] (c) Tomographic reconstruction of radiated power during a detached phase of H-mode with deuterium and nitrogen injection in ASDEX Upgrade. During pronounced detachment a radiating zone inside the confined plasma at the X-point has clearly developed. [Reprinted courtesy of Reference [31]

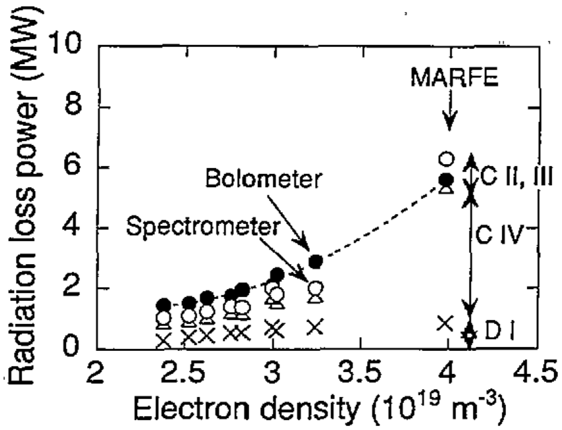

Figure 4. Radiation los in the divertor region of JT-60U measured by spectroscopy and bolometry as functions of line-averaged density for discharges with 11 MW of neutral beam injection heating. The crosses indicate the radiative losses due to DI, the triangles indicate the sum of the radiative losses due to DI and CIV and the open circles the total radiative losses measured by spectroscopy, DI and CII-IV. The closed circles indicate the radiative losses measured by bolometry. The points at the highest density are data from a detached divertor plasma with a MARFE. [Reprinted courtesy of Ref [33].]

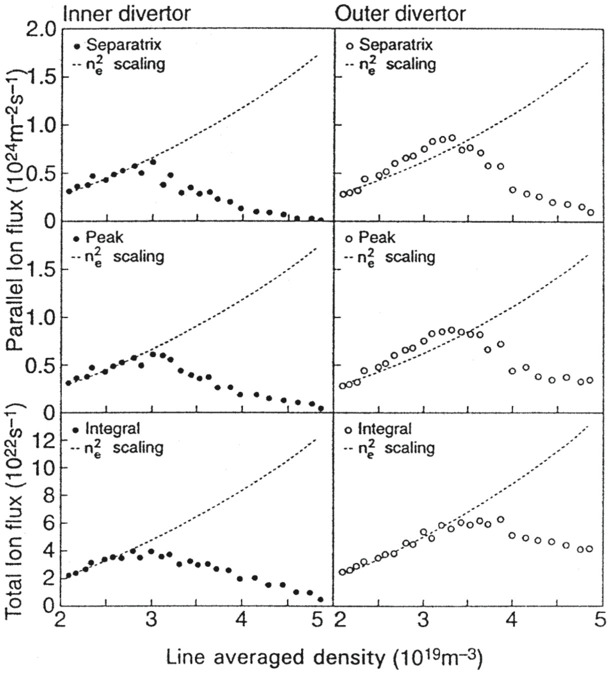

Figure 5. Measured and extrapolated ion fluxes to the inner and outer divertors for an ohmic density ramp in JET. The same quadratic law is used for the separatrix ion flux, the peak ion flux to the divertor and the integral ion flux to both the inner and outer divertor. [Reprinted courtesy of Ref [4]]

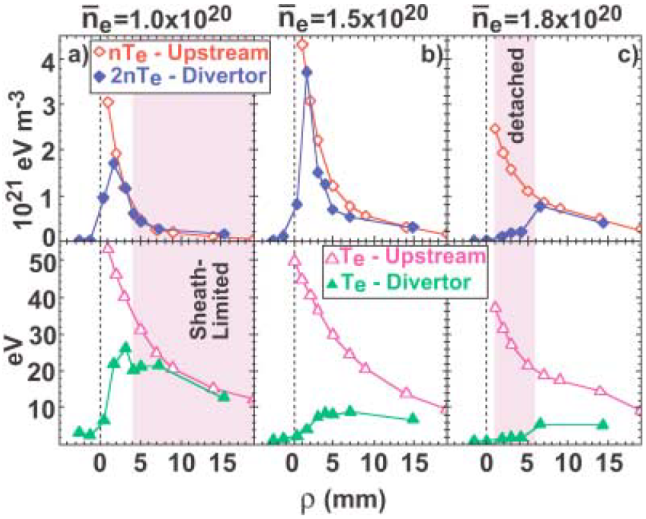

Figure 6. Upstream (OL) and downstream (divertor) profiles of electron pressure and T_e for three different divertor regimes in Alcator C-Mod: (a) low density or sheath limited, (b) high recycling, and (c) detached. [Reprinted courtesy of Reference [46]

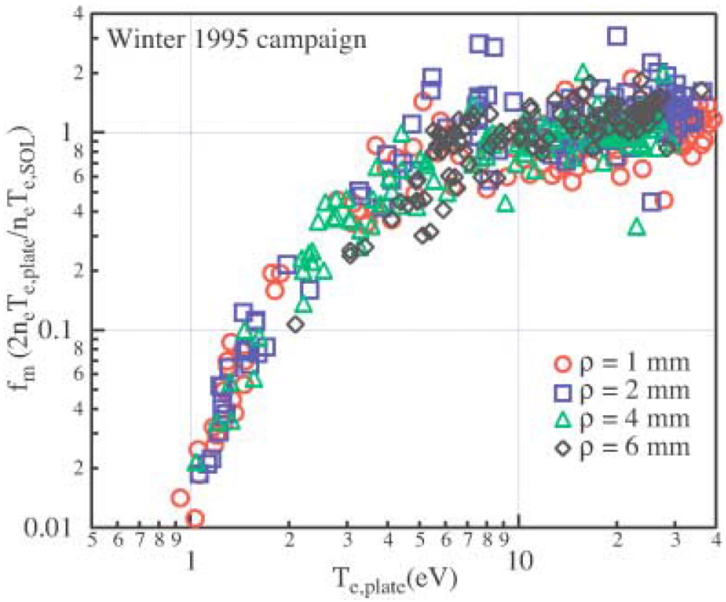

Figure 7. Ratio of electron pressures upstream to that at the divertor plate as a function of divertor plate electron temperature in Alcator C-Mod. Data are shown form a large number of discharges and for four locations outside the separatrix (ρ is the distance from the separatrix referenced to the midplane). [Reprinted courtesy of Reference [43]

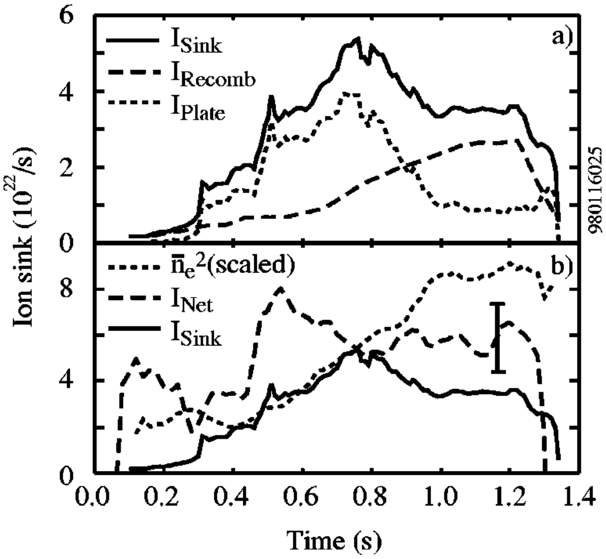

Figure 8. Ion sinks for the outer divertor plate in Alcator C-mod 1 MW Ohmic detached plasmas (starts at ~0.75 s) where $\bar{n}_e$ is increased continuously until 1.0 s. (a) The total ion 'Sink' current is equal to the 'Plate' ion current plus 'Recombination' ion current. (b) The total Sink current is compared to that expected from the '$\bar{n}_e^2$' scaling of the Two-Point model and that expected from the 'Net' power flowing into the outer divertor ionization region converted to ion flux (=P_{net}/e•30 eV). [Reprinted courtesy of Reference [71]]

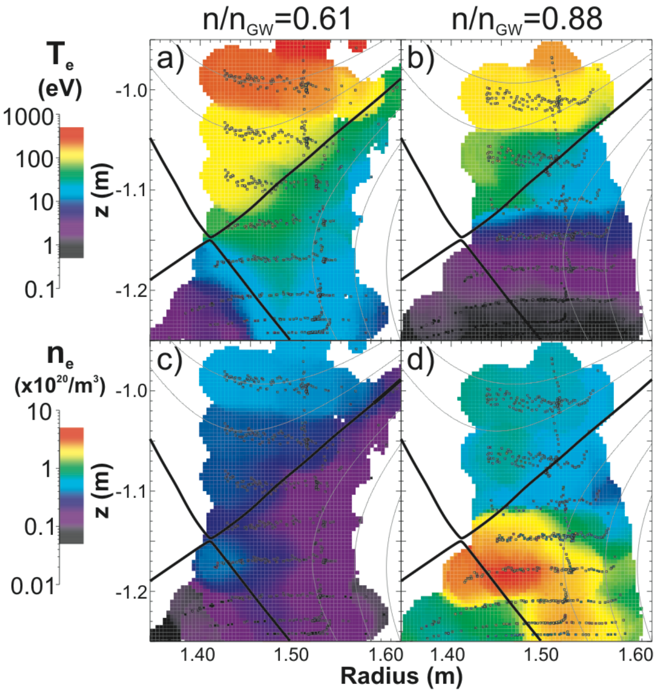

Figure 9. 2D mapped Divertor Thomson Data (DTS) are shown for a low density attached divertor discharge in DIII-D with 2.5 MW of NBI heating (left panels) and similarly for a high density detached divertor discharge (right panels). Individual data points shown by the small squares are used to fit the 2D profile shown as the color contour. The magnetic flux surfaces outside the separatrix are separated by $\Delta\psi_n$=0.004. [Reprinted courtesy of Reference [50]

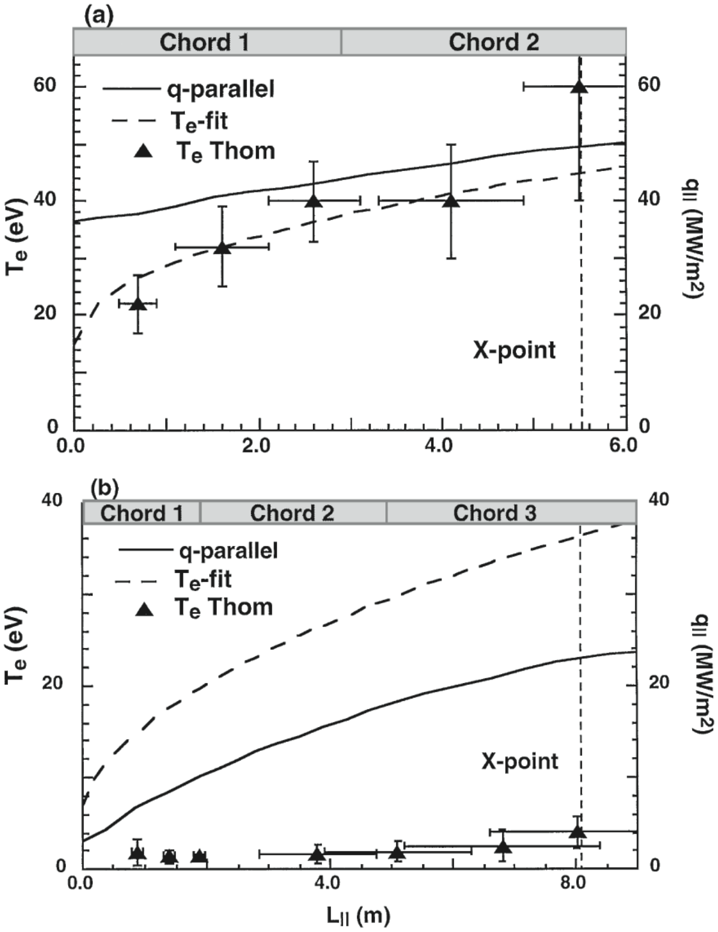

Figure 10. Outboard divertor parallel energy flux analysis in DIII-D for (a) standard ELMing H-mode between ELMs and (b) detached divertor plasma. Shown as a function of the parallel distance from the target, $L_{||}$, are the parallel energy flux, $q_{||}$, the fitted T_e profile from Thomson scattering and the expected T_e profile if electron conduction dominated parallel transport. Shown at the top of each graph are the approximate view locations of the horizontal viewing bolometer chords used for calculation of $q_{||}$. [Reprinted courtesy of Reference [72]

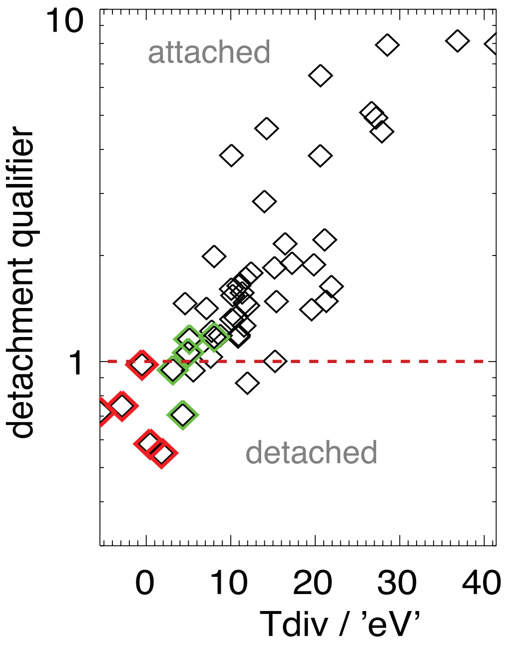

Figure 11. Detachmnt qualifier versus $T_{e,div}$ for discharges with D fueling or dominant N seeding. The red symbols represent pronounced detachment and the green symbols partial detachment. [Reprinted courtesy of Reference [31]]

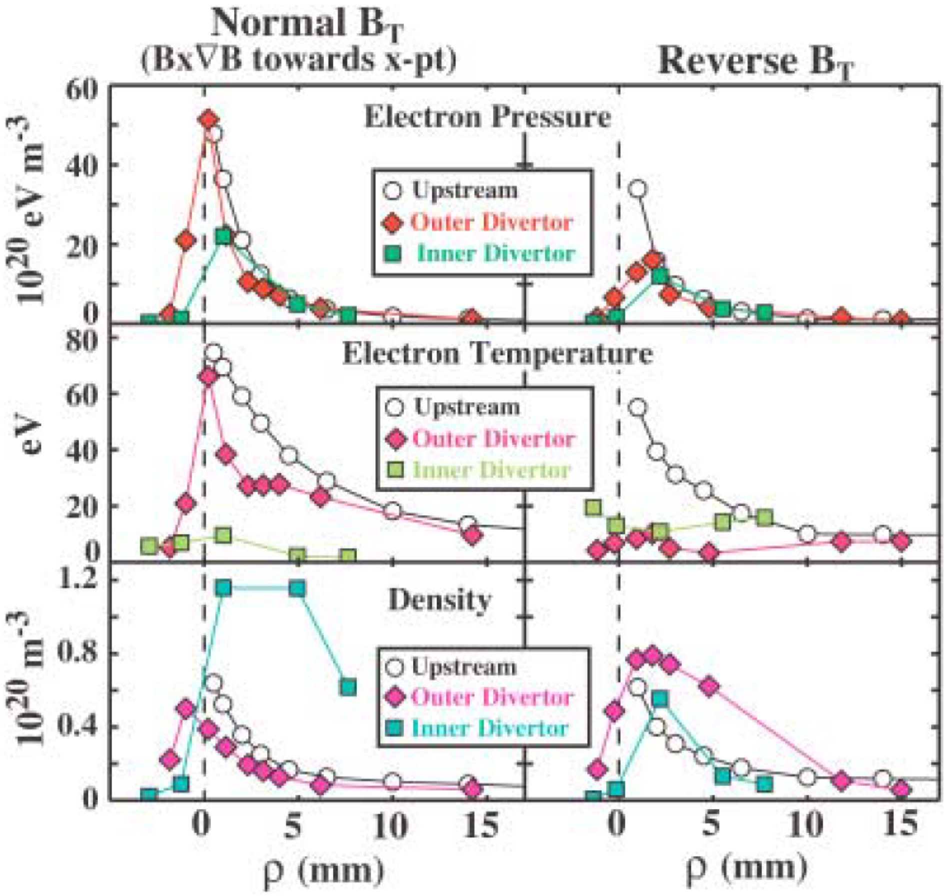

Figure 12. Electron pressure, temperature and density profiles in Alcator C-Mod at the scanning probe location (outboard SOL above the X-point) and on the inner and outer divertor surfaces for forward and reversed B_T directions, shown for a set of 800 kA, lower single-null, ohmic plasmas. [Reprinted courtesy of Reference [46]]

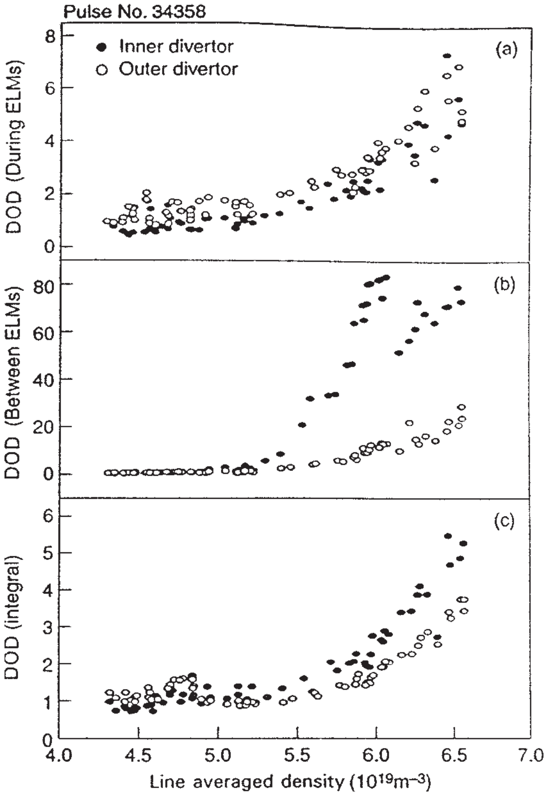

Figure 13. In JET Mark I divertor (a) measured peak degree of detachment during ELMs and (b) between ELMs for an H-mode density scan. This is characteristic of detachment in H-modes, where the inboard divertor is detached between ELMs and reattached at the ELMs. The integral degree of detachment (c) includes ELMs in its calculation. [Reprinted courtesy of Reference [4]]

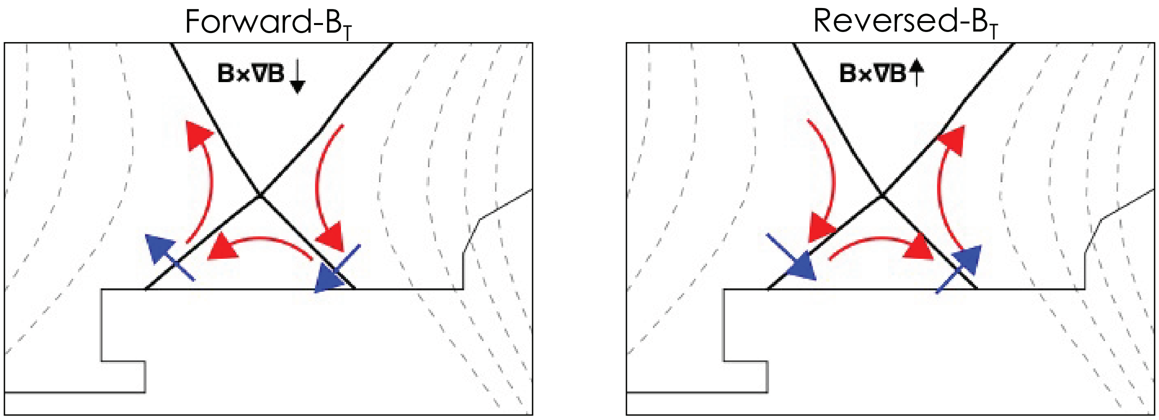

Figure 14. The plasma $\vec{E}\times\vec{B}$ drifts in a lower single null configuration for both directions of the toroidal field. The poloidal drifts driven by radial gradients in T_e (including the sheath potential) are shown in red. The radial drifts driven by poloidal gradients in T_e are shown in blue.

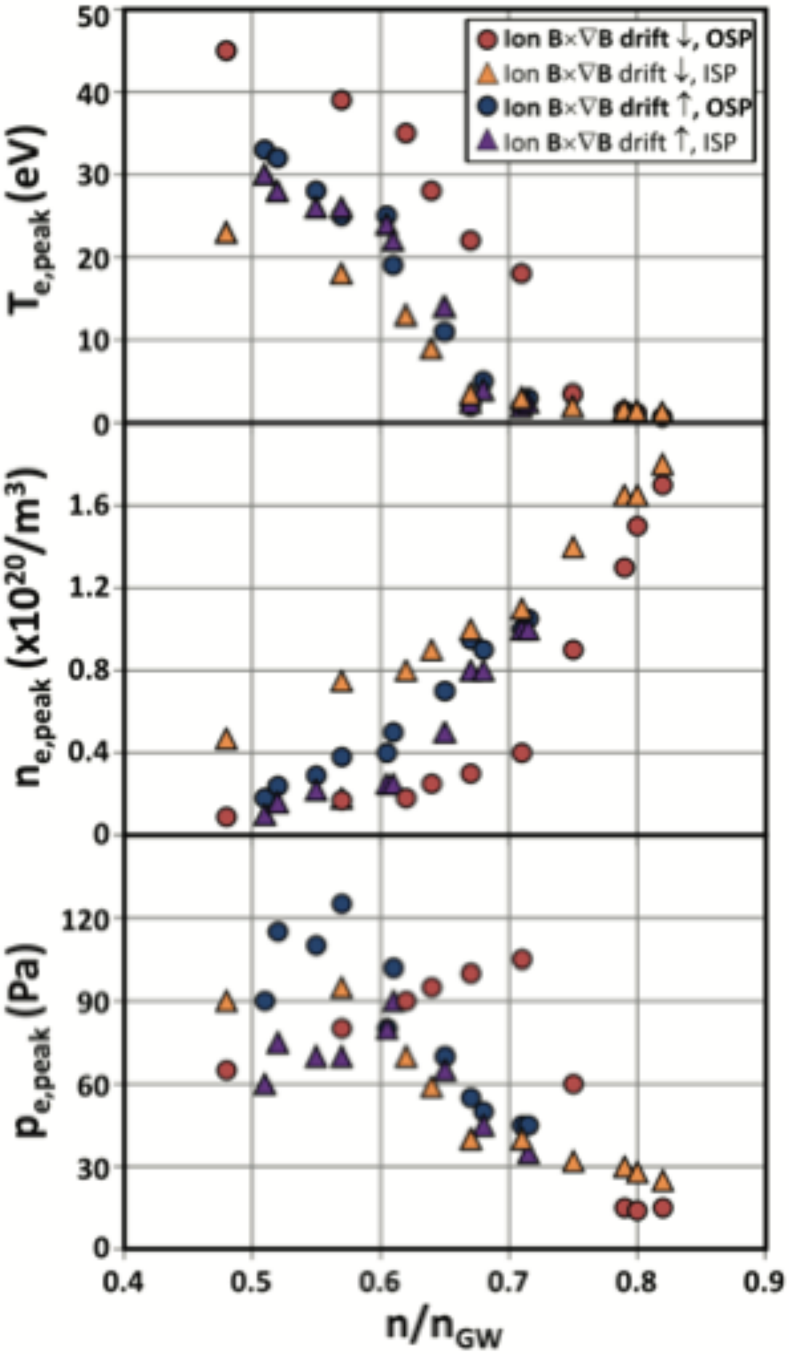

Figure 15. Peak plasma parameters in DIII-D as measured by Thomson scattering at both divertor targets and both B_T directions versus lined-averaged Greenwald

normalized density. Data are shown for T_e (top), n_e (middle) and electron pressure (bottom). Note that peak T_e and n_e do not always occur at the same location in the target profile. [Reprinted courtesy of Reference [103]]

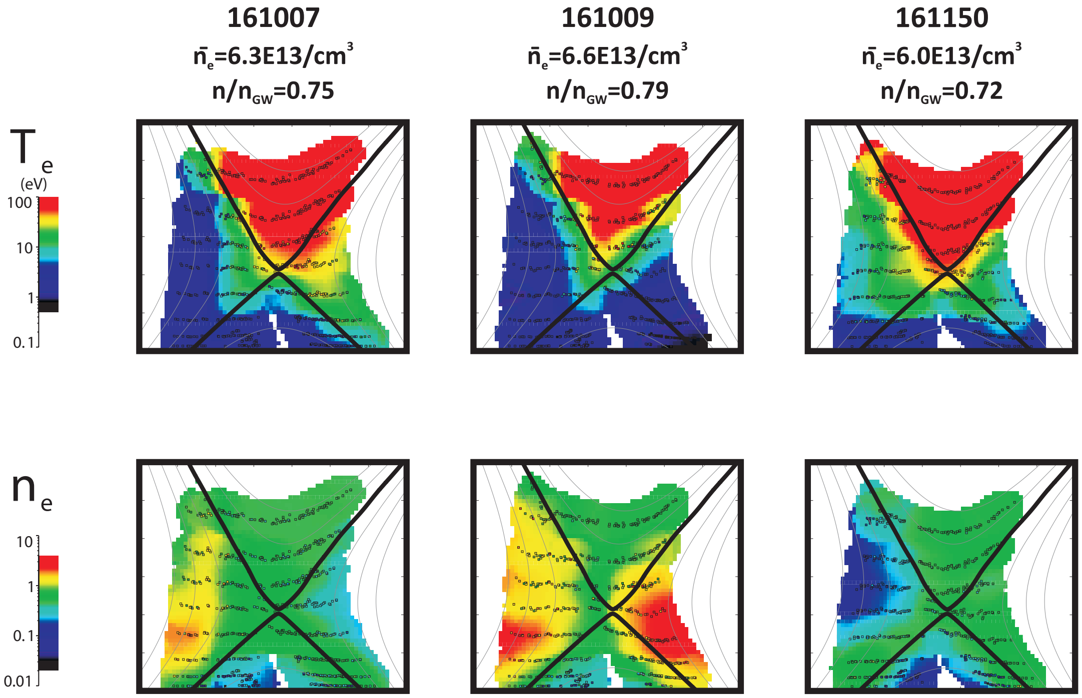

Figure 16. The 2D profiles of divertor n_e (upper row) and T_e (lower row) from Thomson scattering. The color contours are a fit to the individual data points shown with the small squares. Shown are a forward B_t case (□B drift ↓) at a density where the outer strike-point has just begun to detach (left column), a higher density where the outboard divertor is fully detached (middle column) and a reversed B_t case where the outboard divertor detached partway up the divertor leg (right column). [Reprinted courtesy of Reference [103]]

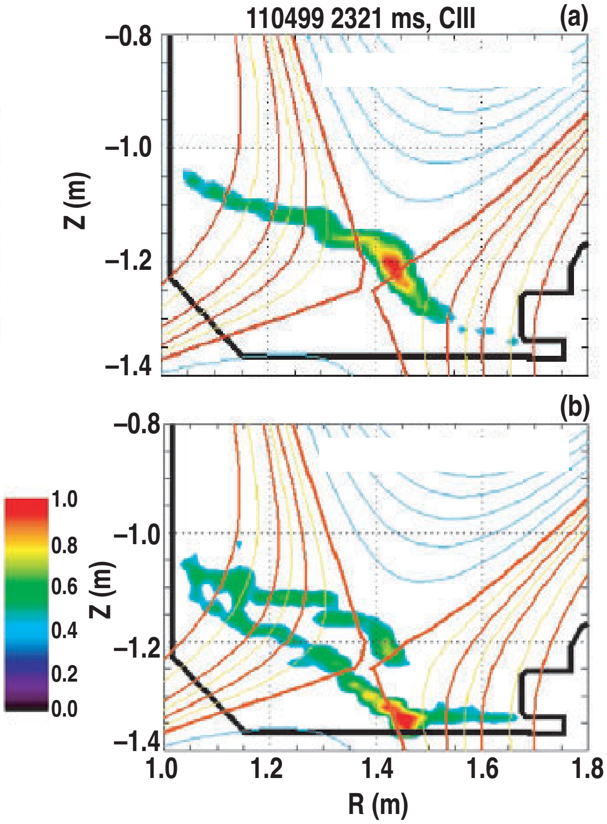

Figure 17. Reconstruction of two-dimensional 465 nm C_{III} emission profiles before (a) and during (b) ELM cycle in the high density case. Image (b) occurs 120 μs later in the ELM cycle than image (a). [Reprinted courtesy of Reference [112]]

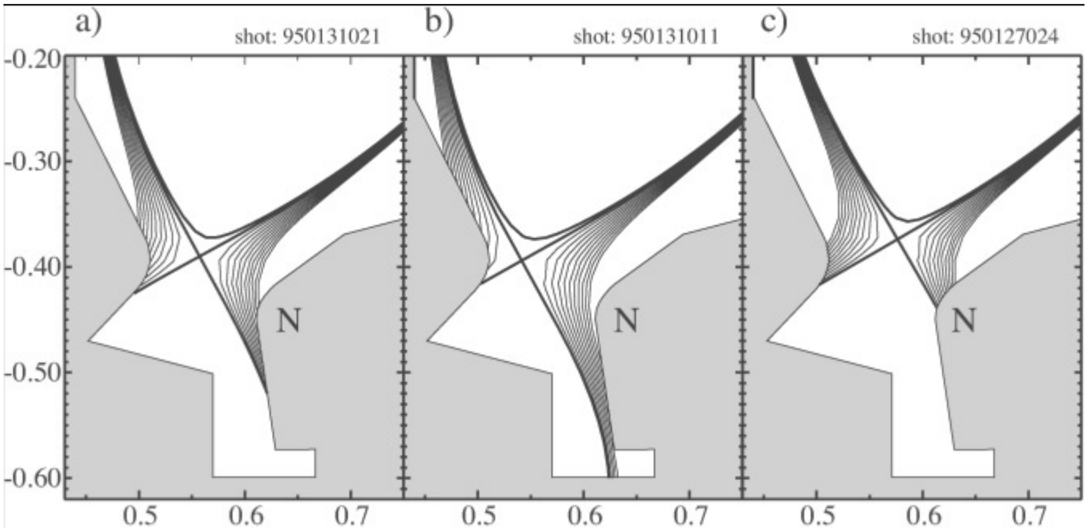

Figure 18. Three divertor geometries in Alcator C-Mod used to investigate the effect of divertor plate inclination on the detachment threshold: (a) standard vertical-plate divertor, (b) slot divertor and (c) flat plate divertor. [Reprinted courtesy of Reference [46]]

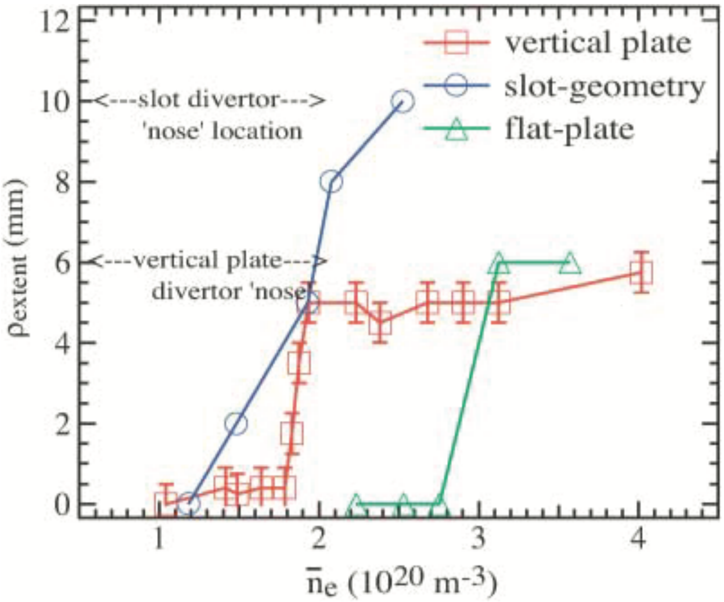

Figure 19. Flux surface extent of divertor detachment as a function of density. For vertical-plate and slot divertor geometries, the detached region extends to the outer divertor nose location. Detachment at the strike-point occurs at $n_e \sim 1.4 \times 10^{20}$ m^{-3} ($n_e/n_{Greenwald} \sim 0.24$) for the slot geometry, at $n_e \sim 1.8 \times 10^{20}$ m^{-3} ($n_e/n_{Greenwald} \sim 0.31$) for the vertical-plate, and at $n_e \sim 2.8 \times 10^{20}$ m^{-3} ($n_e/n_{Greenwald} \sim 0.47$) for the flat plate. [Reprinted courtesy of Reference [46]]

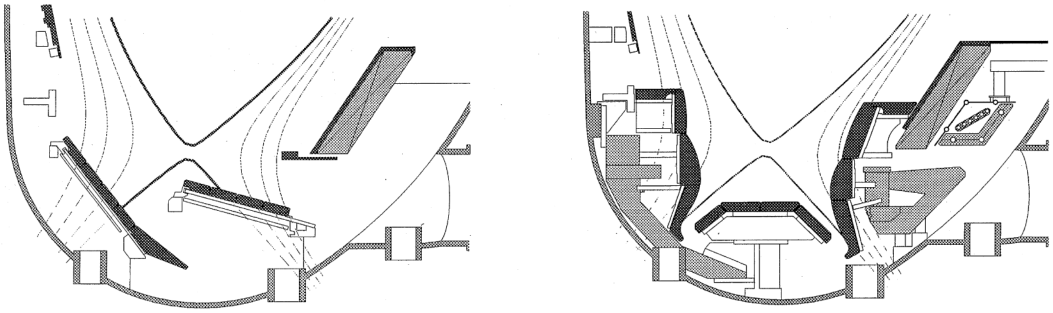

Figure 20. Poloidal cross-section of ASDEX Upgrade with Div-I (left) and Div-II in the Lyra configuration (right). [Reprinted courtesy of Reference [120]]

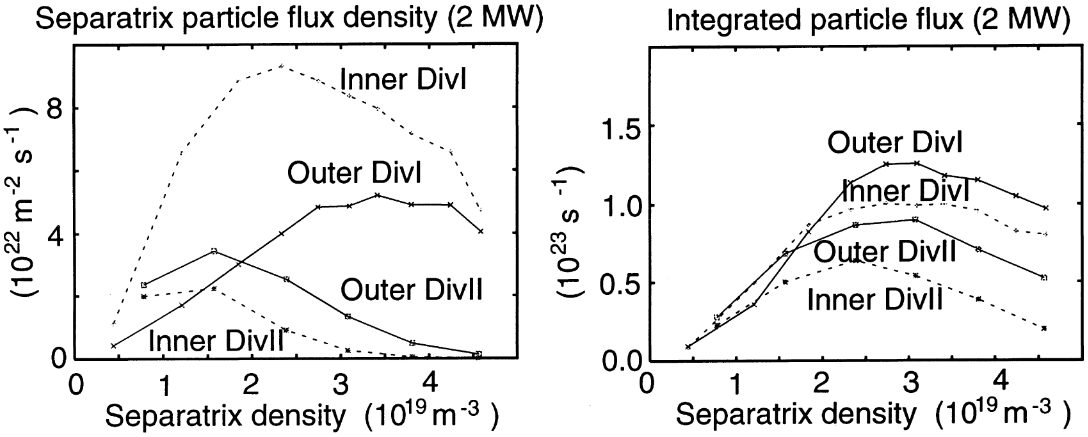

Figure 21. B2-EIRENE density scan for pure hydrogen plasmas with 2 MW input power. On the left side, the dependence of the separatrix particle flux density is shown as a function of midplane separatrix density for inboard and outer target in Div-I and Div-II. On the right side, the same dependence is plotted for the integrated particle flux. [Reprinted courtesy of Reference [120]]

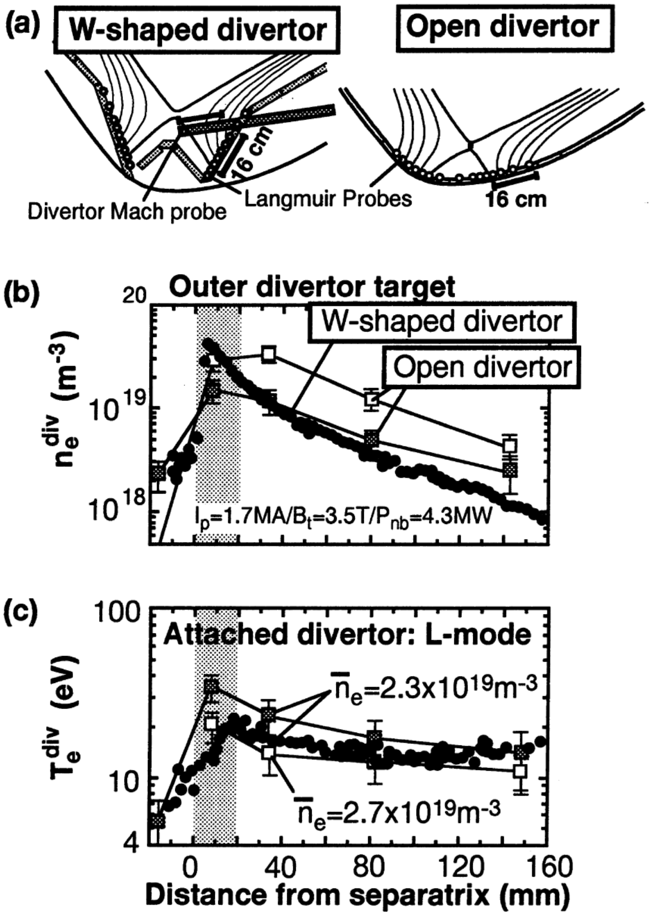

Figure 22. (a) Divertor geometry of the open and the W-shaped divertors. Locations of target Langmuir probes are shown. (b) Electron density and (c) temperature profiles of the outer target. Square symbols show the open diver and the circular symbols show the W-shaped divertor. The profile for the W-shaped divertor is measured during an x-point sweep. [Reprinted courtesy of Reference [47]]

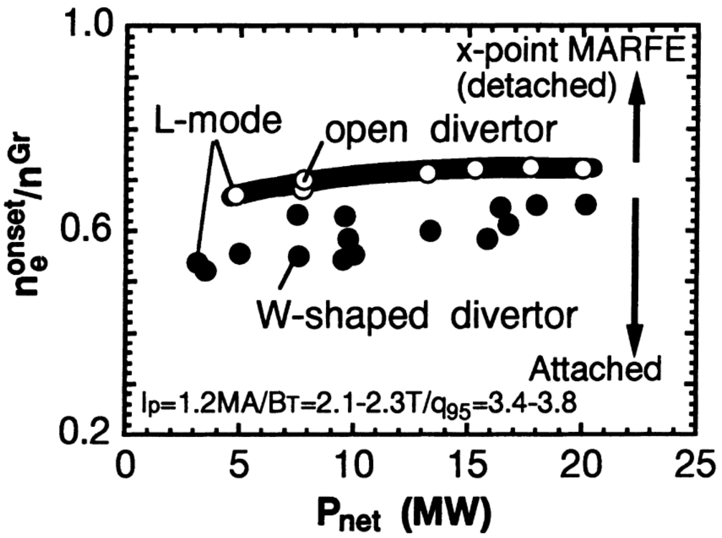

Figure 23. Density of the divertor detachment onset normalized by 'Greenwald density', n^{GR}, as a function of the net input power, P_{net}. Open and closed symbols show the open and W-shaped divertors. Database is for ELMing H-mode except for the noted low power data points. [Reprinted courtesy of Reference [47]]

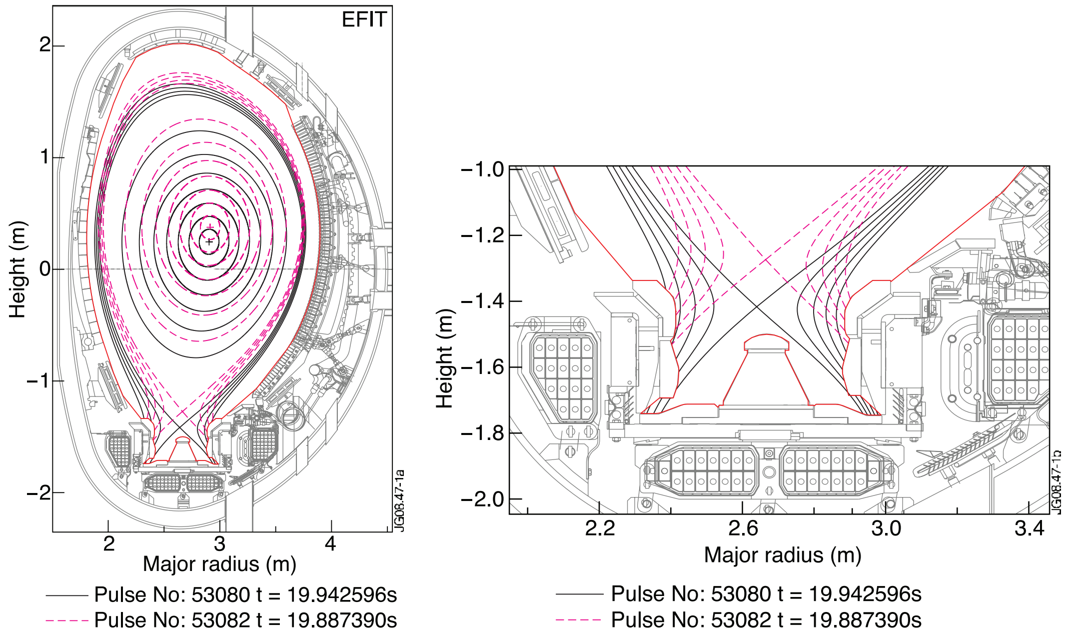

Figure 24. Left: open and closed divertor configurations for high wall clearance magnetic configurations. Right: divertor closeup for the two magnetic configurations. SOL flux surfaces with 5 mm outer midplane spacing. The inner septum outlined in red was removed for later experiments. [Reprinted courtesy of Reference [123]]

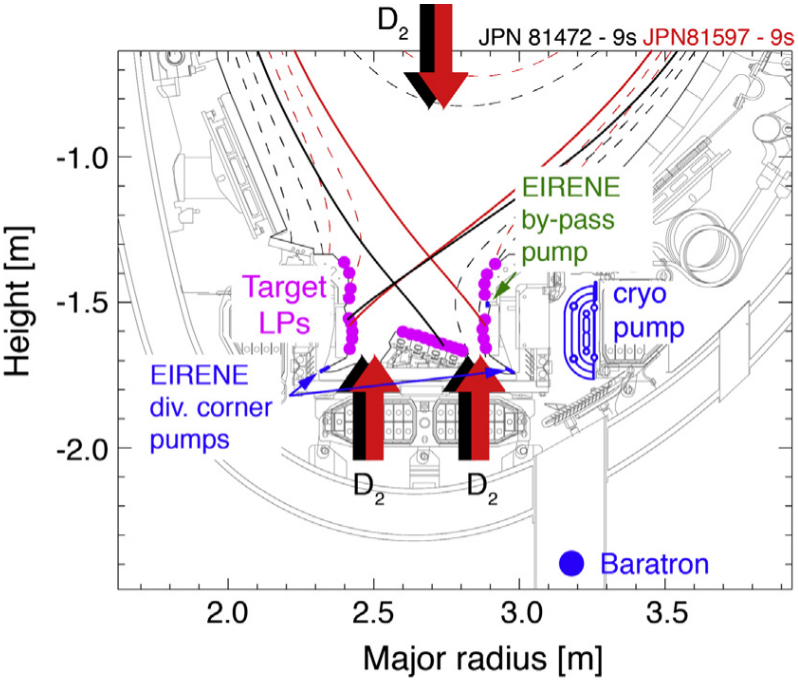

Figure 25. JET divertor and sub-divertor structure and the horizontal (HT, black equilibrium) and vertical (VT, red equilibrium) divertor plasma configurations. Also shown are the divertor Langmuir probes used for divertor plasma characterization. [Reprinted courtesy of Reference [125]]

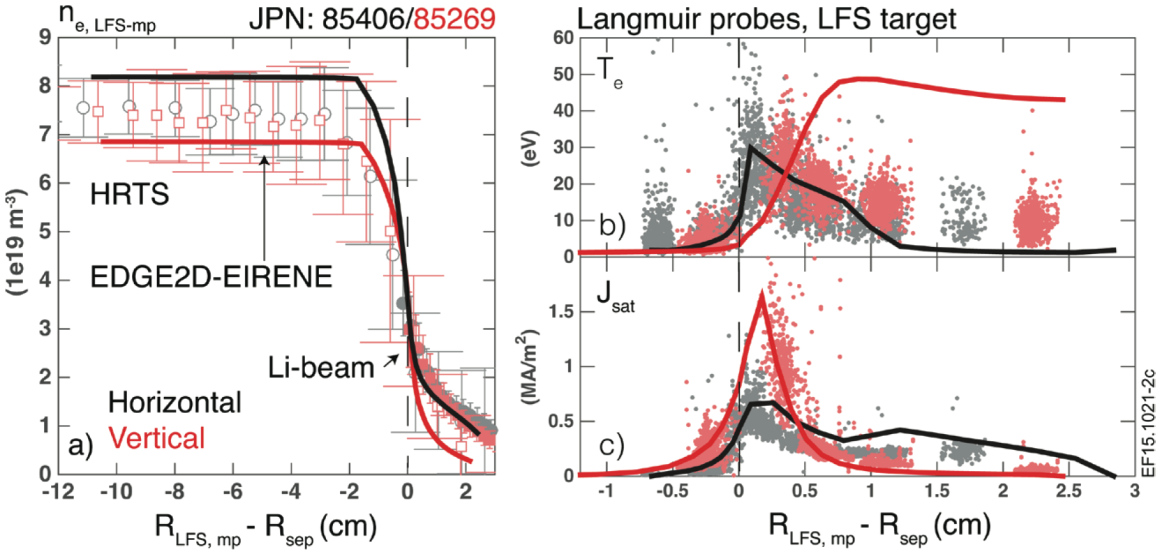

Figure 26. Midplane and divertor conditions for Horizontal (black) and Vertical (red) divertor configurations. (a) Outboard midplane electron density profile from Thomson scattering and Lithium beam diagnostics. (b) Outboard divertor target electron temperature profile from Langmuir probes. (c) Outboard divertor target ion saturation current density from Langmuir probes. EDGE2D-EIRENE modeling

predictions are shown with the solid curves. [Reprinted courtesy of Reference [124]]

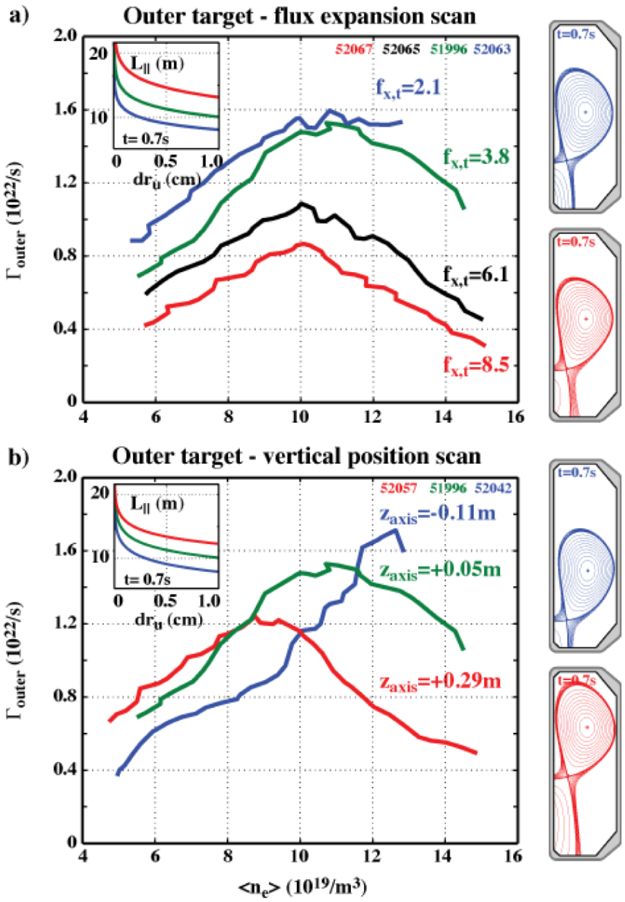

Figure 27. Density dependence of the ion current to the outer target for (a) several flux expansions and (b) several vertical positions. Inserts show the connections lengths. [Reprinted courtesy of Reference [126]]

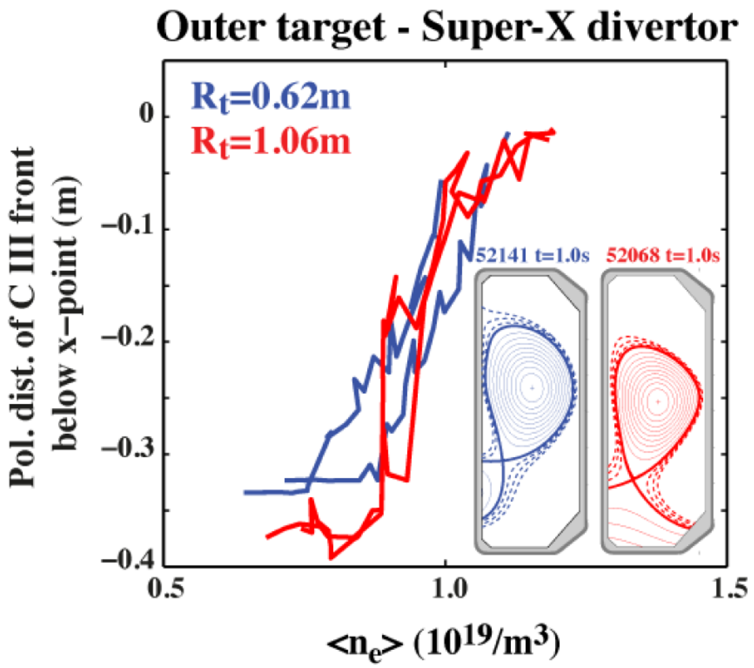

Figure 28. Movement of the CIII cut-off front in density ramps in TCV with different target radii. [Reprinted courtesy of Reference [126]]

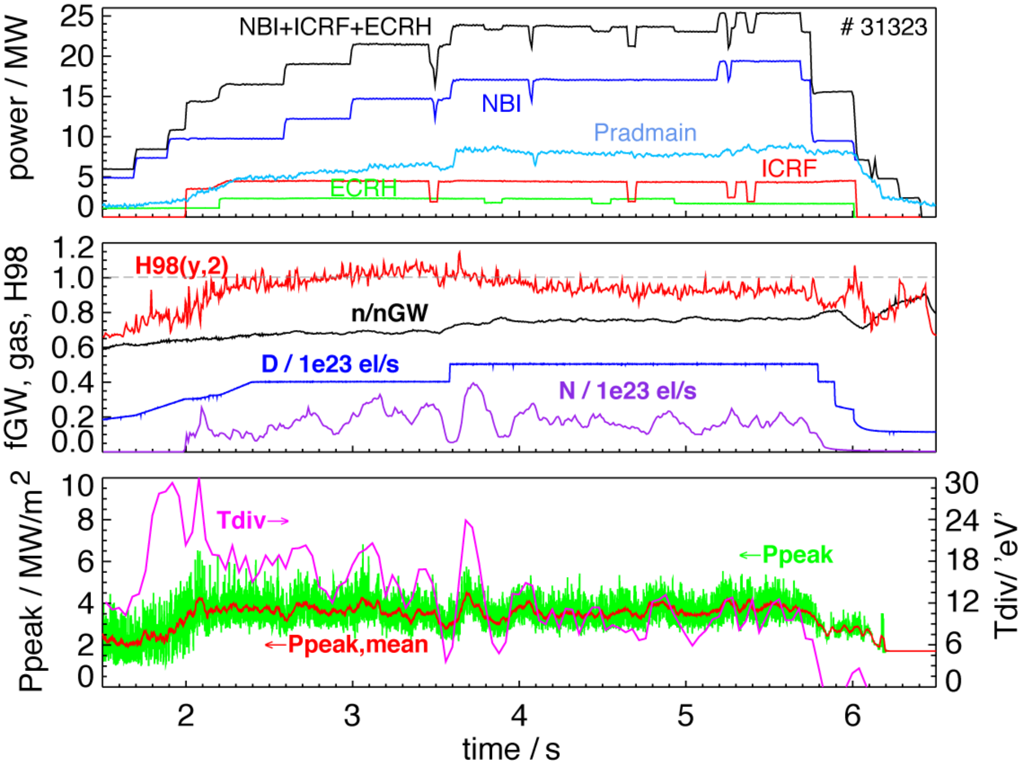

Figure 29. Time traces of an ASDEX-Upgrade discharge with high P_{sep}/R up to 10 MW m^{-1} and a target peak power load around 5 MW m^{-2}. The partially detached conditions are obtained by high deuterium puffing, 1/3 of the nominal cryo-pumping speed and $T_{e,div}$ feedback control using nitrogen divertor puffing. Shown in the first box are the heating powers from NBI, ECRH and ICRF as well as the radiated power in the main chamber. In the second box the normalized confinement, normalized density and deuterium and nitrogen puffing rates are shown. In the third box the divertor T_e measured by the tile currents as will as the peak divertor heat flux are shown. [Reprinted courtesy of Reference [34]]

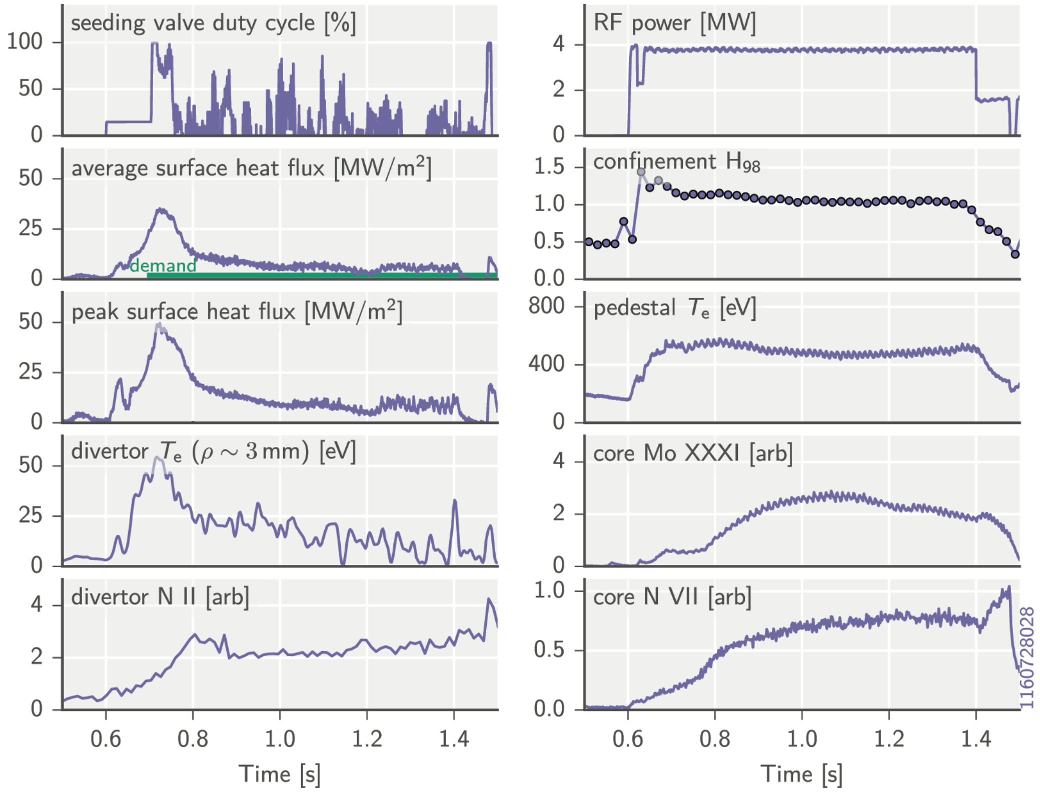

Figure 30. Feedback control of nitrogen impurity seeding during an EDA H-mode on Alcator C-Mod. Peak surface heat flux was controlled down to <10 MW/m^2 while maintaining H_{98}>1. [Reprinted courtesy of Reference [135]]

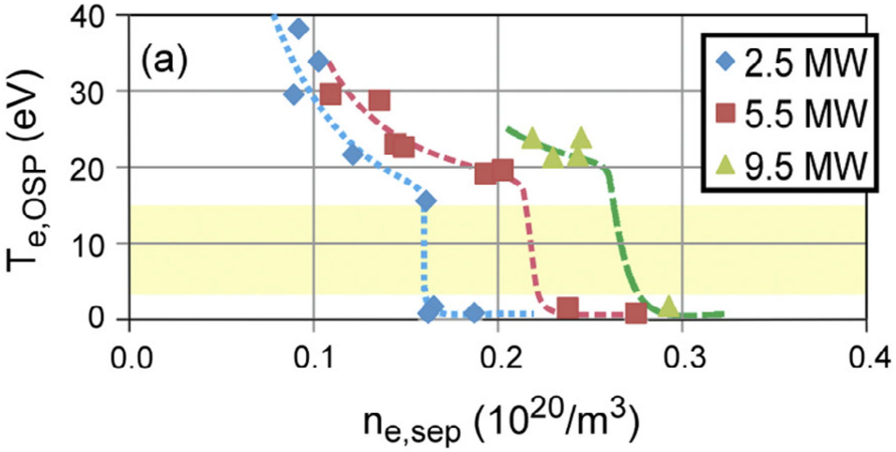

Figure 31. Divertor Thomson scattering measurement of the outboard strike-point T_e as a function of upstream separatrix electron density in DIII-D. Density scans with deuterium injection were carried out for NBI heating powers of 2.5, 5.5 and 9.5 MW. [Reprinted courtesy of Reference [50]]

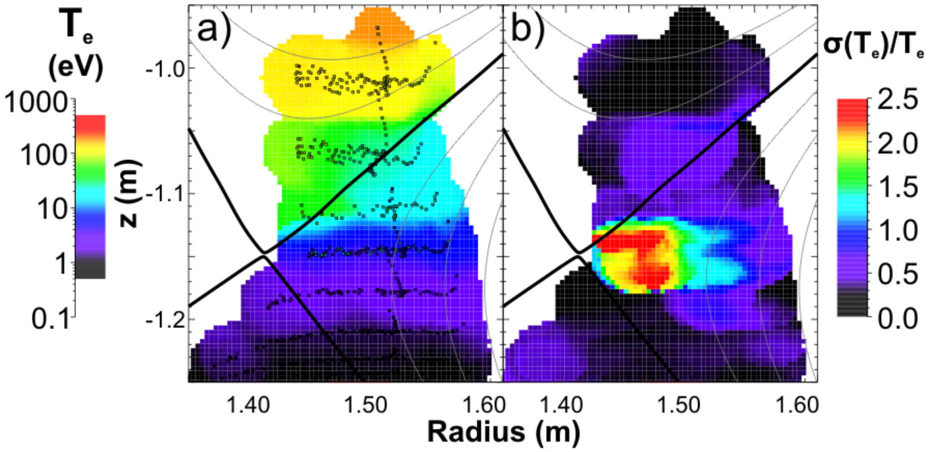

Figure 32. The fitted 2D profiles of divertor (a) T_e and (b) normalized standard deviation of T_e from Thomson scattering measurements in DIII-D. The normalized standard deviation, σ_{Te}/T_e is fitted to the nearby T_e measurements.

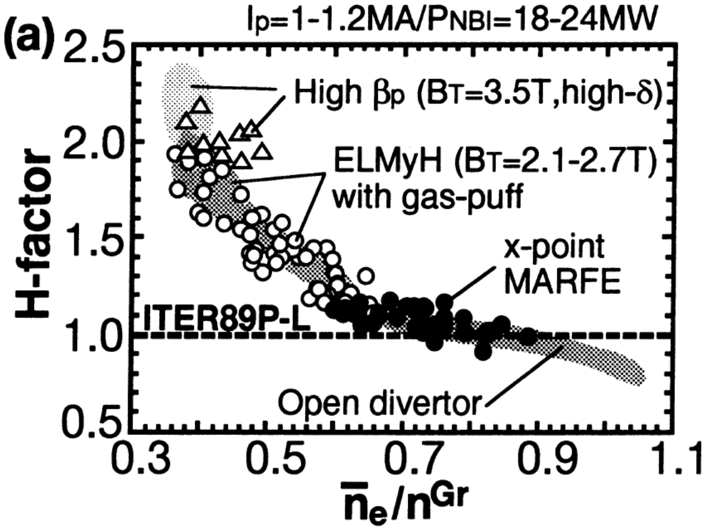

Figure 33. Core confinement H-factor (ITER89P) versus normalized density (n_{GW}) for ELMing H-mode discharges in JT-60U. Symbols and hatched area show database for the W-shaped and open divertors. [Reprinted courtesy of Reference [47]]

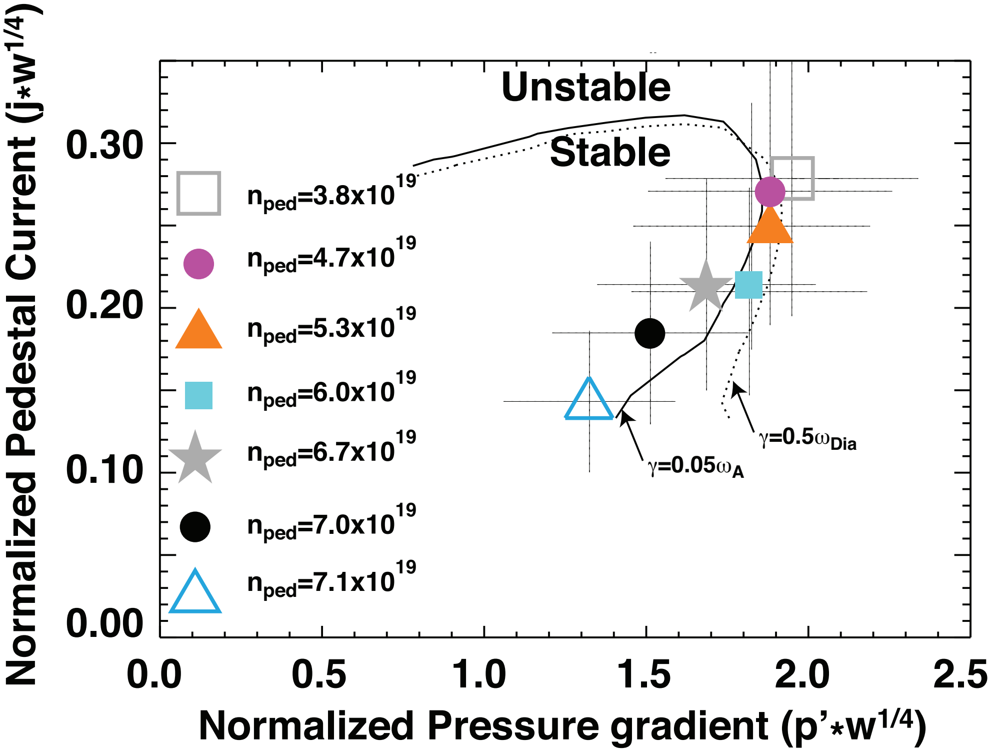

Figure 34. Stability diagram for the edge pedestal current and pressure gradient. The stability space is calculated for the magnetic equilibrium of the $n_{e,ped}=3.8\times10^{19}m^{-3}$ discharge. The pressure gradient and current axes are normalized by the pedestal width, $w^{1/4}$ to allow display of the density scan discharges on the same diagram. [Reprinted courtesy of Reference [144]]

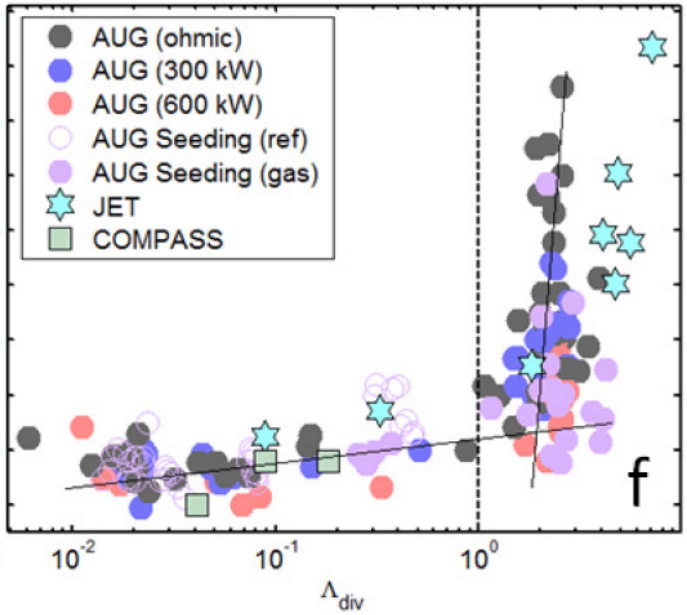

Figure 35. The outboard far SOL density scale length as a function of divertor collisionality from a multi-machine study. [Reprinted courtesy of Reference [152]]